

# 1. Introduction

## 1.1 Background

Demands for increased performance and accuracy are being placed on global geodetic networks. The Hartebeesthoek Radio Astronomy Observatory (HartRAO) Space Geodesy Programme operates from a site in close proximity to cities and industrial areas, which are sources of air and light pollution as well as Radio Frequency Interference (RFI). Cloud cover and obsolete instrumentation also adversely affect geodetic data quantity and quality at the current site. This has necessitated the establishment of a new fundamental space geodetic observatory in South Africa (Combrinck *et al.*, 2007). The space geodetic observatory will host state-of-the-art equipment at a site suitable for optimal scientific output with the current site of choice being Matjiesfontein. A Satellite/Lunar Laser Ranging (S/LLR) system is under development and will form part of the geodetic instrumentation to be located at Matjiesfontein.

The LLR technique is used to measure the distance to the Moon – an LLR system on the Earth transmits a beam of laser pulses to one of several retro-reflector arrays on the Moon with the aim of measuring the round-trip time-of-flight of reflected return photons and calculating the distance travelled. The LLR's laser beam becomes diverged and the beam energy profile is adversely affected during propagation from the Earth to the Moon and back. To be successful, LLR requires optimal optical (/astronomical) seeing conditions, which will allow for the propagation of a laser beam through the atmosphere without excessive beam degradation. Site characterisation should therefore include determination of astronomical seeing conditions for various locations on-site as well as overall atmospheric conditions (Combrinck *et al.*, 2007).

### 1.1.1 Space geodesy

The following description is partially based on a report by the Committee on the National Requirements for Precision Geodetic Infrastructure, Committee on Seismology and Geodynamics and National Research Council (2010):

Geodesy is the science of measuring many aspects of the Earth - its size, shape, rotation, orientation and gravitational field - and other geodynamic phenomena such as crustal and polar motion as well as ocean tides. Space Geodesy is geodesy utilising extra-terrestrial objects such as artificial satellites, the Moon and quasars as reference points, allowing for measurement and representation of the Earth in three-dimensional time-varying space. Space Geodesy helps in understanding the Earth-Atmosphere-Oceans systems interaction.

Space geodesy techniques allow for determining station position, Celestial and Terrestrial Reference Frames (CRF and TRF), Earth Orientation Parameters (EOP), Earth rotation and gravity field, time, tectonic plate motion, tropospheric parameters, orbits of satellites as well as the Moon's distance, orientation and motion, amongst others. These data products are influenced by processes such as crustal motion, earthquakes and volcanism, ocean and atmospheric circulation, weather and climate, solid Earth and ocean tides, sea and ice sheet level changes and postglacial rebound, allowing scientists to model these processes.

Four major space geodesy techniques are used to measure Earth crustal dynamic parameters at sub-centimetre accuracy, with each of these techniques having its own unique observable:

- Geodetic Very Long Baseline Interferometry (VLBI) allows for determining distances between radio telescopes in a global network with an accuracy of several millimetres. This is inferred from varying arrival times of a quasar signal at the different radio telescopes.
- The Global Navigation Satellite System (GNSS) allows for determining antenna-satellite distances from the arrival times of GNSS satellite signals at receiver antennas on Earth, and also allows for determining three-dimensional position, velocity and time.
- Doppler Orbitography and Radiopositioning Integrated by Satellite (DORIS) is a technique whereby signals are transmitted from beacons on the Earth to satellites in orbit. From the observed Doppler shift, satellite orbits and station positions can be determined.

- Satellite/Lunar Laser Ranging (S/LLR) allows for determining the range between a ground station and a satellite (SLR) or the Moon (LLR) by transmitting laser pulses from the ground station to a satellite or Moon. The pulses are reflected back to the ground station's telescope by retro-reflectors placed on the satellite or Moon. By measuring the round-trip time-of-flight of the laser pulse, the position of the satellite or station or Moon can be determined with sub-centimetre accuracy.

Although each space geodesy technique has its own unique strength, all techniques work in synergy and for many final products, a combination of several techniques is used.

### 1.1.2 Lunar Laser Ranging

Lunar Laser Ranging is made possible by retro-reflector arrays deployed on the Moon during the Apollo 11, 14 and 15 missions as well as by retro-reflectors onboard two parked Soviet Lunakhod rovers (Figure 1.1 and Figure 1.2).



Figure 1.1. Location of LLR targets on the the Moon (source: NASA).



Figure 1.2. A retro-reflector array on the Moon's surface (source: NASA).

At a laser ranging observatory on Earth, powerful laser pulses are aimed through a large telescope and directed at the retro-reflectors on the Moon's surface. It is reflected back to the telescope at the observatory and the return signal time is measured. The round-trip travel time of a pulse allows one to translate it to the distance between the observatory and

the retro-reflector on the Moon. This is then translated to centre of mass (Earth) to centre of mass (Moon) for most data products (Combrinck *et al.*, 2007).

Currently there are only four operational LLR stations in the world, namely the Apache Point Observatory Lunar Laser-ranging Operation (APOLLO) in New Mexico and the McDonald Laser Ranging Station (MLRS) near Fort Davis in Texas, both in the United States of America (USA), the Observatoire de la Côte d'Azur (OCA) in Grasse, France, as well as the Matera Laser Ranging Observatory (MLRO) in Italy. At the Wettzell fundamental station in Bavaria, Germany, a lunar laser ranging system is under development. The aforementioned LLR stations are all located in the Northern Hemisphere. In the near-term, the only LLR in the Southern Hemisphere will be located in South Africa.

The accuracy of LLR allows for precise monitoring of the Moon's motion around the Earth, and the Moon's and Earth's relative acceleration towards the Sun, enabling verification of the Strong Equivalence Principle postulated in the theory of General Relativity. It also allows evaluation of the value of the gravitational constant  $G$ , in particular the estimation of the first order derivative of  $G$ . In addition to the Earth-Moon distance, LLR has also provided information about the structure and dynamics of the Moon and that of the Earth, such as (Dickey *et al.*, 1994) –

- the Moon's rotation rate, and motions caused by the Sun's and Earth's gravitational forces, provide evidence that the Moon possesses a small (radius  $< 350$  km) liquid core;
- tidal friction is slowing the Earth's rotation causing the length of an Earth day to change by about 2 milliseconds per century, causing the Moon's orbit to expand at a rate of  $\sim 3.8$  cm per year.

### **1.1.3 The need for a new fundamental space geodetic observatory**

Space Geodesy in South Africa is operated from HartRAO as a base. HartRAO is situated in a valley in the Magaliesberg hills, approximately 50 km north-west of Johannesburg. Both radio astronomy and space geodetic research are performed at HartRAO. The

HartRAO Space Geodesy Programme focuses on the four major space geodesy techniques - VLBI, GNSS, DORIS and SLR (Figure 1.3). Long-term monitoring of Earth processes with these four space geodesy techniques from the very same site provides a trusted long-term data record. The co-location of the four space geodetic techniques makes HartRAO one of only five fiducial geodetic sites worldwide. It is also the only fundamental station in Africa. Located in Africa as well as the Southern Hemisphere, the station position is of strategic importance in the worldwide space geodesy network (Combrinck and Combrink, 2004).

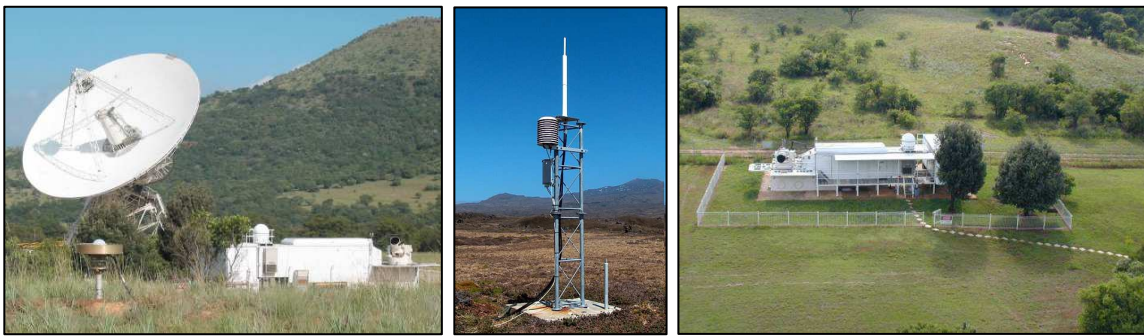


Figure 1.3. Space geodesy at HartRAO – VLBI, GNSS, DORIS (Marion Island) and SLR (MOBLAS-6).

Geodetic equipment at HartRAO is ageing and experiences more downtime than before. The HartRAO 26-m radio telescope does not meet VLBI2010 requirements for a future geodetic VLBI system. Currently, only 15% of telescope time is allocated to geodetic VLBI, whereas VLBI2010 requires continuous 24-hour VLBI observations. Currently, HartRAO operates at S (13 cm / 2.3 GHz) and X (3.5 cm / 8.6 GHz) bands only, while VLBI2010 requires operating up to 14 GHz. Another drawback of the current site at HartRAO is the increased pollution from the ever advancing city boundaries. It creates both RFI as well as deteriorating visibility of the sky at the site, limiting geodetic data quantity and quality. Also, cloud covered summer skies do not allow for optimal scientific output where laser ranging is concerned. The global geodetic network will be weakened considerably should HartRAO not participate in future space geodetic developments such as dedicated geodetic VLBI antennas, kilo-Hertz (kHz) SLR, densification of GNSS networks and near real-time data dissemination (Combrinck and Combrink, 2004; Combrinck *et al.*, 2007).

Increased performance and accuracy are demanded from global geodetic networks. It has become apparent that HartRAO needs to build additional outstations. Establishing a new fundamental space geodetic observatory in a location suitable for optimal scientific output has been proposed (Combrinck and Combrink, 2004; Combrinck *et al.*, 2007). All four main space geodetic techniques should be hosted on-site at a single location. The observatory will be equipped with advanced instrumentation. An LLR system is under development and will form part of the geodetic instrumentation at the new site. In an S/LLR collaboration with OCA in France, a 1-m aperture Cassegrain telescope has been donated by OCA to HartRAO (Figure 1.4). It will have to be refurbished before installation and a new generation LLR system will have to be designed and built to utilise this telescope.



Figure 1.4. The OCA 1-m aperture Cassegrain telescope mount and tube at HartRAO.

The new fundamental space geodetic observatory is to be deployed on a site most suitable for high quantity and quality data output, i.e. a site with a benign atmosphere and reduced RFI. According to Combrinck *et al.* (2007), site requirements include:

- Stable bedrock – Location on deep soils or expansive clays would bias short-term and long-term results. Installation of a superconducting gravimeter and precision GNSS receiver to detect solid Earth movements would allow for modelling of Earth-tide, pole-tide, ocean and atmospheric loading motion and the vertical motion of the site to

be determined. This combination would enable the use of site-specific models, in particular by using Love numbers which are ‘tuned’ to a specific site.

- Protection from RFI – Locating the site in a protected valley would reduce chances of RFI from sources such as cellular phones and microwave ovens.
- Dry, clear and non-turbulent skies presenting good astronomical seeing conditions – Earth's atmosphere absorbs and distorts light and radio waves. Installation of a weather station and seeing monitor with state-of-the-art instruments to map parameters such as pressure, cloud coverage and seeing conditions.
- Low horizon cut-offs – Open sky is required for early source acquisition. An average horizon level of  $\sim 15^\circ$  or better is required.
- Accessibility and infrastructure such as roads, electricity and water.
- Internet access and sufficient bandwidth is required for autonomous operation and streaming data.

Investigations into a possible new location for a fundamental space geodetic station started in 2002 (Combrinck and Combrink, 2004). Potential sites within southern Africa identified initially included only Lesotho, Sutherland and Matjiesfontein. Recently Klerefontein and other sites in the Eastern Cape and KwaZulu-Natal have been added to the list of possible sites. A short description of potential sites is provided in Appendix A1.

#### **1.1.4 Astronomical seeing determined by turbulence and optical methods**

Turbulence in the atmosphere causes dispersion and divergence of the LLR's laser beam. Astronomical seeing is a term used to quantify turbulence in the Earth's atmosphere. Image degradation and positional shifts are manifestations of turbulence in the Earth's atmosphere. Plane wave fronts emanating from stars are distorted by index of refraction variations caused by turbulent layers in the atmosphere. From the change in a stellar image relative to that expected under perfect conditions, a quantitative measure of seeing conditions can be derived (Roddiier, 1981; Coulman, 1985; Roggeman and Welsh, 1996). The LLR return signal consists of a small number of photons. Single photon detection from the Moon is a non-trivial task (Combrinck *et al.*, 2007), therefore optimal astronomical seeing conditions of  $\leq 1$  arc-second resolution level is required for ranging success.

Seeing quality is significantly degraded by atmospheric turbulence in the boundary layer (lowest part of the atmosphere affected by interaction with Earth's surface). Integration of methods from instruments measuring astronomical seeing and boundary layer meteorology (models) is necessary to link astronomical seeing conditions with time-space variations of atmospheric properties caused by turbulent processes (Erasmus, 1988; Erasmus, 1996).

## **1.2 Motivation for the research**

As an international facility, the new fundamental space geodetic observatory will be expected to meet international standards for data quantity and quality. Adverse astronomical seeing conditions (atmospheric turbulence) present severe limitations on the quantity and quality of data collected, therefore all space geodesy techniques require a benign atmosphere. For the S/LLR to achieve the required accuracy in tracking calibration stars, satellites and the targets on the Moon, astronomical seeing conditions of  $\leq 1$  arc-second resolution level are required. A very important consideration for a specific site is that the laser beam diverges at a ratio directly proportional to the astronomical seeing conditions. For example, for every 1 arc-second of seeing, the laser beam will have diverged 2 km by the time it strikes the surface of the Moon. Sites with poor seeing conditions would reduce the chance of receiving a sufficient number of return photons to such an extent that LLR would simply not be possible. Calculations for a link budget indicate that for seeing conditions of 2 arc-seconds, only about 5-7 photons per minute would be captured. A proper characterisation of astronomical seeing conditions at the best proposed locations is therefore essential.

## **1.3 Aim and objectives**

A two-pronged approach to determine astronomical seeing conditions at a potential site is proposed – the use of a turbulence-resolving numerical model, the Large Eddy Simulation NERSC (Nansen Environmental and Remote Sensing Centre) Improved Code (LESNIC) (Esau, 2004), to simulate atmospheric boundary-layer structure and behaviour, in conjunction with a seeing monitor for on-site quantitative measurements of seeing conditions (Roddier, 1981).



The overall aim of this study is to determine whether a turbulence-resolving numerical simulation model, such as LESNIC, and an in-house developed seeing monitor can be utilised to determine astronomical seeing as part of site characterisation for a new fundamental space geodetic observatory.

The overall aim will be achieved by the following objectives:

### **OBJECTIVE 1**

**Make use of LESNIC to obtain modelled seeing results and verify these results against observed results obtained during field campaigns as reported in the literature.**

### **OBJECTIVE 2**

**Investigate the optimal design for a seeing monitor and verify scientific functionality of the seeing monitor equipment and techniques employed.**

### **OBJECTIVE 3**

**Investigate how parameters of modelled results obtained with LESNIC may be used in conjunction with measured results from the seeing monitor to predict the seeing at a site.**

## **1.4 Method**

To determine astronomical seeing conditions at a proposed site, a two-pronged approach of simulation and measurement, using methods from both boundary layer meteorology and astronomical seeing, was envisaged. The Large Eddy Simulation (LES) method was extended to calculate turbulence profiles and seeing parameter values and tested using the LESNIC model. Simulated results for turbulence profiles and seeing parameter values were provided by the LESNIC model for a site for which the necessary meteorological data were available. Quantitative seeing measurements were obtained at Matjiesfontein by employing a seeing monitor designed in this study. In a future study (not conducted during this work),

the relationship between modelled and measured seeing conditions at a particular site should be investigated and an integrated system developed.

Cost and availability of equipment dictate the possible methods to be employed for determining astronomical seeing conditions and boundary layer meteorology at a proposed site for the new fundamental space geodetic observatory. Although *in-situ* experimental methods for determining seeing conditions are difficult, time-consuming and expensive, seeing is not stationary and requires near real-time monitoring necessitating continuous operations. It was decided to investigate the possibility of developing an in-house seeing monitor for on-site quantitative measurements of seeing conditions. Double star separation measurements were used for calibration and verification purposes (Napier-Munn, 2008). With this system it is possible to determine the column seeing (the column of the atmosphere through which the telescope is observing and the laser beam is propagating) as would be experienced by an optical telescope or laser beam.

A more general approach to secure data for the huge variety of Planetary Boundary Layer (PBL) states is not possible with the seeing monitor. The use of a turbulence-resolving numerical model, the Large Eddy Simulation NERSC Improved Code (LESNIC) (Esau, 2004), to simulate atmospheric boundary-layer structure and behaviour, was therefore proposed and an appropriate script for calculating turbulence profiles and seeing parameter values was developed.

A model, such as LESNIC, would allow for predicting approximate and general seeing at a site (seeing scenarios), whereas the seeing monitor would make actual measurements to determine column seeing as at the time of measurement. The two techniques are therefore supportive of each other, but one must realise the suitability of each for their particular field of application. A combined approach could be used to rapidly select sites using the LESNIC model, followed with site specific testing using a seeing monitor to determine the better site from the modelled selection.

## 1.5 Study outline

The thesis consists of seven chapters. In Chapter 2, the theoretical background linking astronomical seeing conditions to atmospheric turbulence is provided. Chapter 3 follows with a description of the experimental methodology employed in deriving astronomical seeing from LESNIC and DATABASE64 results, as well as that used in obtaining quantitative seeing measurements with the seeing monitor. The design and automation of a seeing monitor setup, as well as support-infrastructure and -instrumentation required on-site, are described in Chapter 4. In Chapter 5, comparative results for turbulence profiles and seeing parameter values obtained from DB64 (not site-specific) and results measured over Dome C in Antarctica, as well as results from a seeing monitor setup verification test and preliminary results for the PSF technique, are presented. The use of a two-pronged complementary approach to measure and predict seeing at a site is proposed in Chapter 6. The investigation into the suitability of using a turbulence-resolving model such as LESNIC and an in-house developed seeing monitor to characterise astronomical seeing conditions at a site is rounded off in Chapter 7, which contains final conclusions and recommendations.

## **2. Theoretical background to seeing**

### **2.1. Introduction**

In this chapter, the theoretical background of atmospheric turbulence and astronomical seeing is presented. The origin of and processes involved in turbulence generation are discussed, as is the Kolmogorov statistical theory of turbulence (Kolmogorov, 1941) and the refractive index structure parameter, which gives a measure of optical turbulence strength in the atmosphere (Tatarski, 1961). Astronomical seeing is discussed with reference to diffraction- and seeing-limited telescopic observation. Required parameters are introduced to quantify optical seeing quality. Atmospheric turbulence and astronomical seeing are linked to each other through certain parameters.

### **2.2. Atmospheric turbulence**

Atmospheric turbulence, which occurs mostly in the atmospheric layer closest to Earth, the Planetary Boundary Layer (PBL) / Atmospheric Boundary Layer (ABL)), degrades seeing. Turbulence results when the boundary layer between air masses with different temperatures breaks up into local unstable air masses, called eddies (Stull, 1988). The eddies act as weak, irregular lenses causing refractive index variations which can distort electromagnetic wave fronts (Roddier, 1981; Roggeman and Welsh, 1996). The vertical distribution of turbulence is given by the profile of the refractive index structure constant  $C_N^2(h)$  (Tatarski, 1961; Roddier, 1981; Roggeman and Welsh, 1996; Andrews and Phillips, 2005).

#### **2.2.1. Earth's atmosphere**

Earth's atmosphere consists of an envelope of air held near the surface by the Earth's gravitational attraction. This mixture of gases mainly comprises nitrogen, oxygen, argon and carbon dioxide. Spatial-temporal variations in temperature and pressure are used to divide the atmosphere into different layers, namely the troposphere, stratosphere, mesosphere and thermosphere (Figure 2.1). The troposphere is the lowest layer of the atmosphere. Here pressure and temperature decrease with altitude. Most of the turbulence

is also generated here, as most of the weather processes take place in this layer. The troposphere is composed of different molecules, one of which is water vapour, which plays a large role in controlling the troposphere's physical properties and processes. Water vapour drives structural and dynamical processes and carries latent heat for global redistribution of energy.

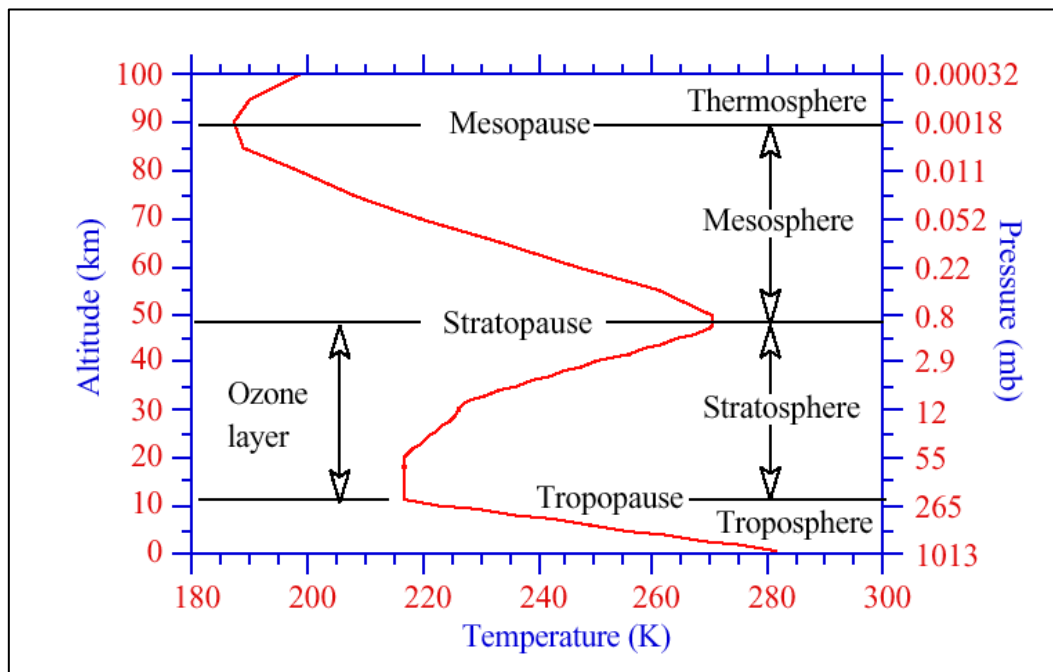


Figure 2.1. Temperature profile in the atmosphere (source: Claire E. Max, University of California, Santa Cruz).

Various forces influence the motion of the atmosphere. There are forces which affect horizontal flow - the pressure gradient force, friction and the Coriolis force, which is due to the Earth's rotation. These horizontal forces change the speed and direction of the wind. There are also forces that affect the vertical motion of the atmosphere - gravity, friction, buoyancy and terrain features all influence the wind's vertical motion.

The PBL is directly influenced by interaction with the Earth's surface and, depending on time of day and weather conditions, varies from surface level up to an altitude of ~ 200 m to 2 km (Trinquet and Vernin, 2006) (Figure 2.2). Turbulence occurs mainly in the surface layer [0 to 100 m], planetary boundary layer [0 to 2 km] and free atmosphere [2 to 30 km]. The most disruptive turbulence occurs near the Earth's surface. The PBL therefore

contributes significantly to the degradation of optical seeing quality. The index of refraction fluctuations affecting astronomical seeing are located mainly in the PBL of the troposphere.

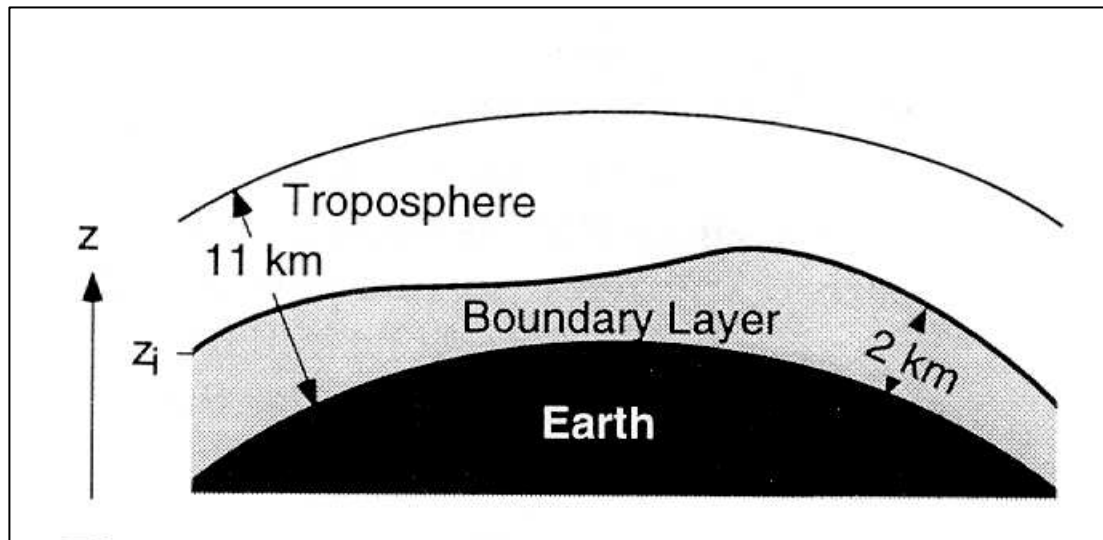


Figure 2.2. Planetary boundary layer (PBL) (source: Stull, 1988).

Turbulence in the PBL is responsible for the vertical transportation of surface turbulent fluxes of momentum, mass as well as sensible and latent heat. Friction acts on the ambient flow, creating wind shears, which are changes in the direction and speed of wind with height. Turbulent eddies are formed by these wind shears. The size of the turbulent eddies is proportional to the size and shape of the obstacles in the wind's path and also depends on the wind's speed. Mean profiles of wind speed, wind direction, temperature and humidity in the PBL are controlled or mixed by turbulent eddies.

The PBL can be divided into four sub-layers: the surface layer, the mixed layer, the stable layer, and the residual layer (Figure 2.3). The surface layer is the sub-layer closest to Earth. Molecular viscosity dominates at centimetre-level close to the surface and above it in this layer, and turbulence is relatively constant and isotropic. A mixed layer forms when turbulent mixing is produced mainly by convective motion. Turbulent motion in the mixed layer is driven by wind shear and buoyancy forcing (Moeng and Sullivan, 1994). Coherent eddies (thermals, plumes, vortices) cause turbulent fluxes of momentum, heat and other scalars such as humidity, gases (e.g. carbon dioxide) and pollutants (Chou and Ferguson,

1991). The residual layer begins to form when turbulence and the mixed layer decay on sunset. This (residual) layer is not directly influenced by the Earth's surface.

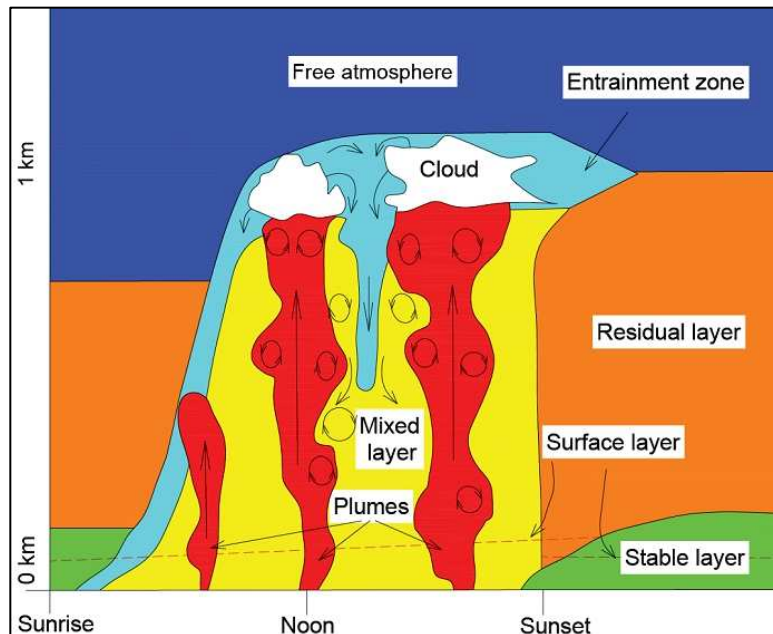


Figure 2.3. The PBL regions (source: University of Wisconsin Lidar Group (adapted)).

As the sun sets, convective motion decreases. The lower part of the PBL is stabilised by radiative cooling and surface friction. A stable boundary layer (SBL), in which turbulence is intermittent and affected by the underlying terrain, is formed. Turbulence in the lower layer of the SBL is locally coherent (Grant, 1992). It is weak, sporadic and contains a large portion of the night-time heat flux (Nappo, 1991).

Generation of turbulence in the PBL is influenced by factors such as energy budgets, moisture, diurnal variations, buoyancy, shear and roughness length. The amount of energy entering and leaving the PBL determines the surface heating. The magnitude of convective turbulence generated in the PBL is determined by this surface heating, while the amount of mechanical turbulence formed in the PBL is determined by wind shear. A rapid change in wind speed and direction causes instabilities and energy cascade of turbulent eddies of different sizes. Heterogeneous surface properties such as water, vegetation, land cover, buildings and forests also influence turbulence in the PBL. These properties create differences in surface fluxes of momentum, heat and moisture. Together with terrain

irregularities, these surface fluxes produce transient eddies, which modify turbulent fluxes within the PBL.

### 2.2.2. Turbulence theory

Image degradation is caused by atmospheric turbulence. In order to understand the optical properties of the atmosphere, it is therefore necessary to understand the processes involved in generating atmospheric turbulence. In his work, A.N. Kolmogorov (1941) founded the field of the statistical analysis of turbulence. The Kolmogorov theory of turbulence was further developed by Obukhov (1941), Tatarski (1961), Fried (1965) and Fried (1966). The following discussion of Kolmogorov turbulence is based on descriptions that can be found in Tatarski (1961), Roddier (1981), Roggeman and Welsh (1996) as well as Andrews and Phillips (2005), the latter work having been referred to extensively. In the Kolmogorov model of turbulence (Kolmogorov, 1941) (Figure 2.4), it is assumed that the medium is incompressible and that small-scale turbulence is homogeneous and isotropic. Energy is added on the largest scales, transferred to progressively smaller scales and dissipated by viscous action. This cascade process is responsible for variations in temperature and density, which leads to refractive index variations.

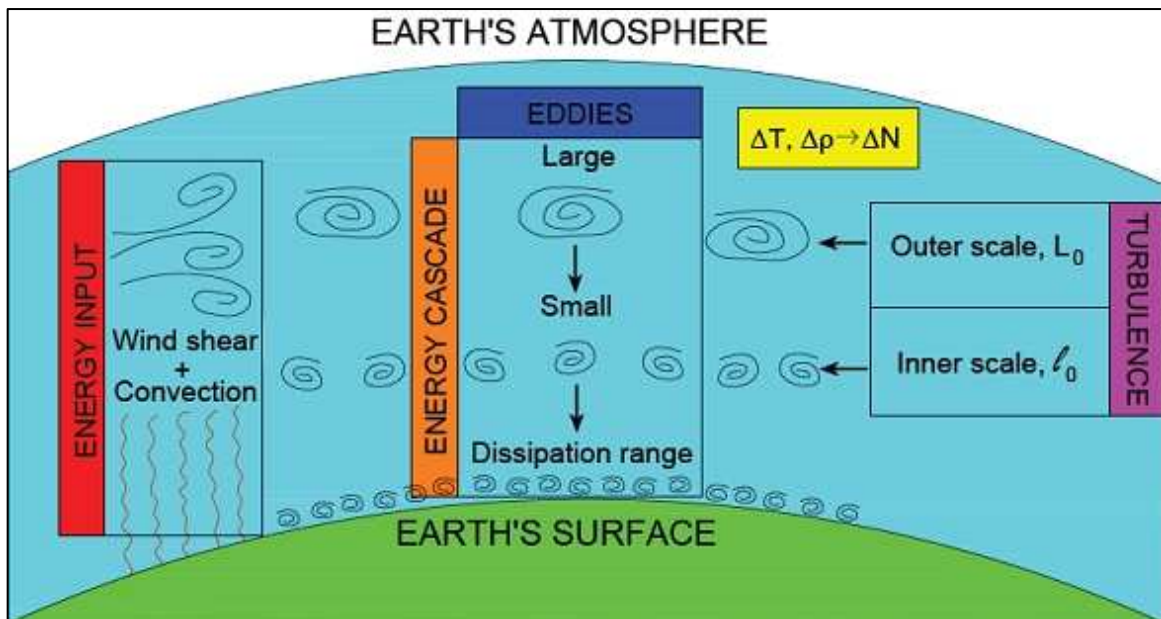


Figure 2.4. Kolmogorov model of turbulence.



The atmosphere, which can be treated as a viscous fluid, displays either laminar or turbulent flow. Turbulent flow is not stable or linear, but chaotic, and it is characterised by mixing. Eddies with different temperatures are mixed by wind and convection and break up into smaller structures. The mixing produces fluctuations in density and therefore in the refractive index of air. Eddies have large and small scales referred to as the outer scale of turbulence  $L_0$  and the inner scale of turbulence  $l_0$ , respectively. Here  $L_0$  ranges from  $10 - 10^2$  m and has wind shear or convection as energy source. Small scale eddies are too small to impart energy to the flow but large enough to avoid energy dissipation by friction. The inner scale of turbulence  $l_0$  is on the order of a  $10^{-3}$  m in size. Eddies with scale sizes smaller than the inner scale (Kolmogorov scale) are subject to viscous dissipation and belong to the dissipation range. Thus, energy flows from  $L_0$  to  $l_0$  and is dissipated by friction.

The Reynolds number  $Re$  gives the critical value at which the flow of a viscous fluid changes from laminar to turbulent. When dynamic forces of flow exceed damping forces of viscosity, the Reynolds number exceeds the critical value and turbulence results. The flow becomes unstable, forming vortices, which grow large enough to interfere with neighbouring eddies and is dominated by chaotic interactions between the eddies. The Reynolds number  $Re$  is a dimensionless quantity given by

$$Re = \frac{VL}{\nu} \left( \frac{[m.s^{-1}][m]}{[m^2.s^{-1}]} \right), \quad (2.1)$$

where  $V$  and  $L$  represent characteristic velocity and length scales of the flow and  $\nu$  is the kinematic viscosity.

Kolmogorov introduced structure functions to provide a statistical description of the random processes involved in turbulence. With turbulence, variables such as velocity, temperature, pressure and humidity are non-stationary and therefore do not have well-defined averages. By making use of stationary increments it is possible to find well-defined averages of the differences between the values. A structure function is an example of this type of quantity and allows for determining the intensity of fluctuations over a short time scale. A structure function is thus a measure of the intensity of fluctuations of a non-

stationary random variable over a short time scale. The structure function  $D_x(R)$  of a random variable  $x$  (e.g. temperature, index of refraction etc.), measured at two points separated by distance  $R$ , is defined by

$$D_x(R) = \left\langle (x_1 - x_2)^2 \right\rangle. \quad (2.2)$$

Kolmogorov's theory of turbulence was developed considering velocity fluctuations of the turbulent field. Kolmogorov introduced the longitudinal velocity structure function, parallel to the vector  $\vec{R}$  connecting two points separated by distance  $R$ , to describe velocity field fluctuations

$$D_v(R) = \left\langle (V_1 - V_2)^2 \right\rangle, \quad (2.3)$$

where  $V_1$  and  $V_2$  [ $\text{m}\cdot\text{s}^{-1}$ ] are velocities measured at two points separated by distance  $R$ , and the triangle brackets denote ensemble averages. A similar expression applies to any conservative, passive additive such as temperature (temperature fluctuations do not exchange energy with the velocity field). By extending the Kolmogorov theory of the structure function to statistically homogeneous and isotropic temperature fluctuations, the structure function of the temperature field is similarly described by

$$D_T(R) = \left\langle (T_1 - T_2)^2 \right\rangle, \quad (2.4)$$

where  $T_1$  and  $T_2$  [K] are temperatures measured at two points separated by distance  $R$ , and the triangle brackets denote ensemble averages.

In order to derive a universal description for the turbulence spectrum, Kolmogorov proposed that, in locally isotropic turbulence, the cascade of energy from large scales to smaller scales leads to a statistically self-similar model that depends only on two parameters, the energy dissipation rate  $\varepsilon$  and the kinematic viscosity  $\nu$ . Kolmogorov used a dimensional analysis argument combining these parameters to form characteristic time, velocity, and length scales, which were then used to derive the velocity structure function. Assuming isotropic and homogeneous turbulence, and arguing that the structure function of the velocity field must be independent of viscosity in the inertial range (where dissipation does not play a role), the Kolmogorov-Obukhov two-thirds power law for the velocity field (Kolmogorov, 1941; Obukhov, 1941) is given by

$$D_V(R) = C_V^2 R^{2/3} \quad l_0 \ll R \ll L_0, \quad (2.5)$$

where  $C_V^2$  [ $\text{m}^{4/3}\text{s}^{-2}$ ] is a measure of the total amount of energy in the turbulence for separation distance  $R$  (which falls between the inner and outer scales of turbulence) between the two velocity measurements of Equation (2.3). This power law gives turbulence strength as a function of eddy size, the spatial correlation of turbulence decreasing in proportion to the two-thirds power of the spatial separation. The relationship is only valid for  $R$  in the inertial sub-range. By extending the Kolmogorov theory of the structure function to statistically homogeneous and isotropic temperature fluctuations, a similar two-thirds power law relation is found for the temperature field and is given by

$$D_T(R) = C_T^2 R^{2/3} \quad l_0 \ll R \ll L_0, \quad (2.6)$$

where the temperature fluctuation constant, also known as the temperature structure parameter,  $C_T^2$  [ $\text{m}^{-2/3}$ ] represents the thermal strength of the turbulence for separation distance  $R$  between the two temperature measurements of Equation (2.4).

### 2.2.3. Index of refraction structure parameter, $C_N^2$

As for the previous section, the following discussion and derivations follow the description in Andrews and Phillips (2005). The vertical distribution of turbulence, also known as the profile of the refractive index structure parameter  $C_N^2(h)$ , is a measure of the fluctuations in the refractive index field, and thus of the strength of optical turbulence responsible for image degradation. The index of refraction in air depends on temperature, pressure and water vapour content. At optical wavelengths, temperature fluctuations dominate water vapour fluctuations in contributing to refractive index fluctuations. Temperature and pressure variations are caused by velocity fluctuations. Pressure variations are rapidly smoothed out by sound waves, but conduction takes much longer to smooth out the variations in temperature. Temperature thus provides the important link between turbulent velocity and index of refraction  $N$ .

Analogous to the structure functions of the velocity and temperature fields, the structure function of the optical field is given by

$$D_N(R) = \left\langle (N_1 - N_2)^2 \right\rangle, \quad (2.7)$$

where  $N_1$  and  $N_2$  are the atmospheric refractive index measured at two points separated by distance  $R$ , and the triangle brackets denote ensemble averages. The Kolmogorov-Obukhov two-thirds power law of Equation (2.5) also describes the structure function of the refractive index fluctuations in the inertial sub-range, which is given by

$$D_N(R) = C_N^2 R^{2/3} \quad l_0 \ll R \ll L_0, \quad (2.8)$$

where the refractive index structure parameter  $C_N^2$  [ $\text{m}^{-2/3}$ ] represents the strength of optical turbulence for separation distance  $R$  between the two refractive index measurements of Equation (2.7). The wave is assumed to maintain a single frequency as it propagates, therefore time variations are not taken into account.

At optical wavelengths, the index of refraction for the atmosphere is given by

$$N - 1 \cong 79 \times 10^{-6} \frac{P}{T}, \quad (2.9)$$

where  $P$  is the pressure in hectopascal [hPa] and  $T$  the temperature in Kelvin. Refractive index fluctuations with respect to temperature variations are obtained by differentiating Equation (2.9) to give

$$\frac{\partial N}{\partial T} = \frac{-(79 \times 10^{-6})P}{T^2}. \quad (2.10)$$

The index of refraction and temperature structure parameters are obtained by combining Equation (2.7) with Equation (2.8) and combining Equation (2.4) with Equation (2.6), respectively, to give

$$C_N^2 = \frac{\left\langle (N_1 - N_2)^2 \right\rangle}{R^{2/3}} \quad (2.11a)$$

and

$$C_T^2 = \frac{\left\langle (T_1 - T_2)^2 \right\rangle}{R^{2/3}}, \quad (2.11b)$$

where  $\left\langle (N_1 - N_2)^2 \right\rangle$  and  $\left\langle (T_1 - T_2)^2 \right\rangle$  represent ensemble averages of index of refraction fluctuations,  $N_1$  and  $N_2$ , and temperature fluctuations,  $T_1$  and  $T_2$ , respectively, at two points separated by a distance  $R$ .

Combining the two equations for the index of refraction and temperature structure parameters as described in Equation (2.11a) and Equation (2.11b), respectively, with Equation (2.10), gives

$$C_N^2 = \frac{\langle (N_1 - N_2)^2 \rangle}{\langle (T_1 - T_2)^2 \rangle} C_T^2 = \left( \frac{\partial N}{\partial T} \right)^2 C_T^2 = \left( 79 \times 10^{-6} \frac{P}{T^2} \right)^2 C_T^2, \quad (2.12)$$

which provides the index of refraction structure parameter  $C_N^2$  in terms of the temperature structure parameter  $C_T^2$  and ambient pressure  $P$  and temperature  $T$ .

The profile of the index of refraction structure parameter with height  $C_N^2(h)$  was derived by Tatarski (1961) as

$$C_N^2(h) = \left( 79 \times 10^{-6} \frac{P(h)}{T^2(h)} \right)^2 C_T^2(h), \quad (2.13)$$

where  $C_N^2(h)$  may be assumed constant for a given height  $h$  above ground and over small time scales at fixed propagation distance. The unit for both  $C_N^2$  and  $C_T^2$  is  $\text{m}^{-2/3}$ , while  $P$  is measured in hectopascal [hPa] and  $T$  is measured in Kelvin [K]. It is difficult to measure  $C_N^2$  directly. Rather, at a given height  $h$ , fast-response thermometers are employed to measure  $C_T^2$  and, together with the measured values of ambient temperature and pressure for that height  $h$ , are used to determine  $C_N^2$ . Values for  $C_N^2$  usually range from  $10^{-17} \text{ m}^{-2/3}$  up to  $10^{-13} \text{ m}^{-2/3}$ , for weak and strong turbulence, respectively.

### 2.3. Astronomical seeing

The relationship between atmospheric turbulence and seeing quality is described in Tatarski (1961), Fried (1965), Fried (1966), Roddier (1981), Coulman (1985), Roggeman and Welsh (1996), Erasmus (1986), Erasmus (1988) and Erasmus (2000). From Section 2.2, it follows that, through index of refraction fluctuations, atmospheric turbulence can result in perturbations of electromagnetic wave fronts (Figure 2.5). For astronomical observations, these perturbations cause electromagnetic wave fronts from extra-terrestrial sources to undergo refraction, absorption, dispersion, blurring etc.

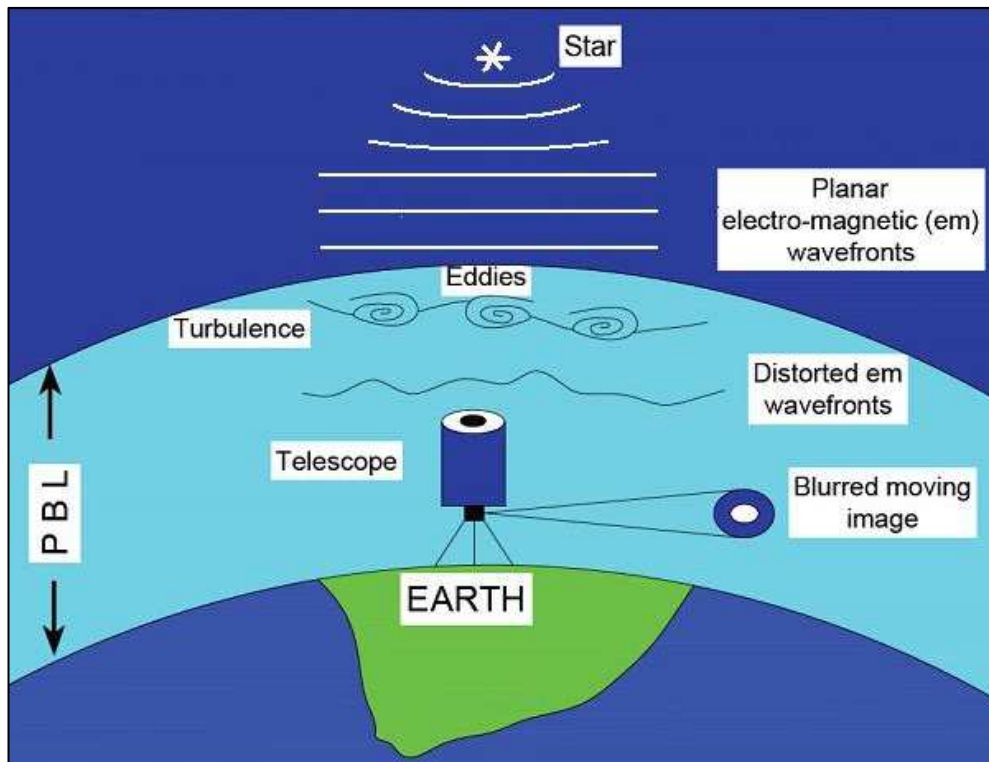


Figure 2.5. Degradation of image quality by turbulence.

Stars are located at an immense distance from the Earth and should therefore appear as no more than point sources when observed through a telescope (or by the naked eye). However, using a telescope on Earth, a star is observed as a blurred, moving image. Although image quality can be affected by the instrument's diameter and quality of optical components, the main contributor to the distortion is atmospheric turbulence.

The degradation of the image quality relative to that expected under ideal conditions provides a measure of the seeing conditions. Although a telescope's theoretical angular resolution, the Rayleigh limit, may be smaller than an arc-second, the image resolution will be limited further by atmospheric seeing conditions. For the purpose of seeing tests, one would usually choose a telescope large enough so that aperture is not the limiting factor for image quality. The smallest resolvable angle in such a setup will then provide the seeing used to measure seeing conditions in optical astronomy.

### 2.3.1. Diffraction limit of telescope

The following explanation for diffraction-limited telescopic observation is based on Léna (1986), Longair (1992) as well as Born and Wolf (1999). Stars, although point sources, do not form point images in the focal plane. Stars rather form discs due to diffraction of the light by lenses, mirrors and other internal components of the telescope. The light passing through the telescope's objective is diffracted. Under perfect seeing conditions, the light forms a bull's eye diffraction pattern (Figure 2.6). The diffraction pattern consists of light and dark rings with a small bright disc, the Airy disc, in the centre. The Airy disc, together with the concentric rings surrounding it, is known as an Airy pattern. The Airy disc represents the central maximum of the diffraction pattern and is the smallest point to which a light beam can be focused. Nearly 84% of light is concentrated in the Airy disc with the remainder contained in the light rings.

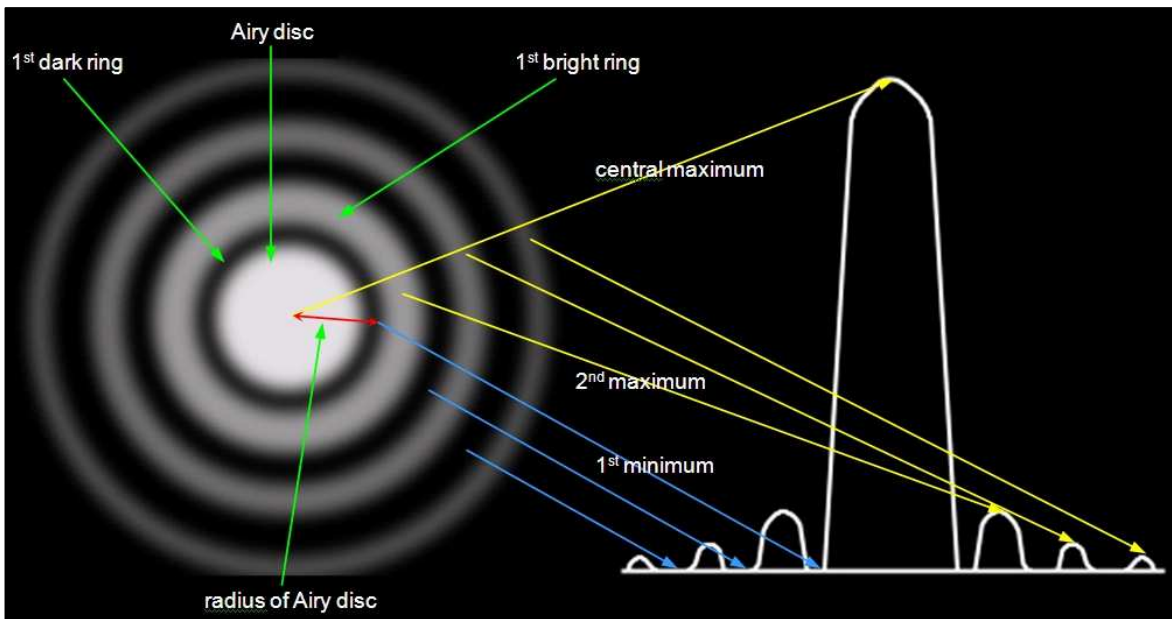


Figure 2.6. Diffraction pattern of star image through a telescope and profile of image brightness (source: <http://starizona.com> (adapted)).

The intensity of the diffraction pattern of a circular aperture, or Airy pattern, is given by the Airy function

$$I(\theta) = I_0 \left[ \frac{2J_1(ka \sin \theta)}{ka \sin \theta} \right]^2 = I_0 \left[ \frac{2J_1(x)}{x} \right]^2, \quad (2.14)$$

where  $I(\theta)$  is the intensity of radiation at observation angle  $\theta$  from the axis of the circular aperture,  $I_0$  is the central intensity of the Airy pattern,  $J_1$  is a Bessel function of the first kind of order unity,  $k = 2\pi / \lambda$  is the wave number,  $a$  is the radius of the circular aperture, and  $x = ka \sin \theta$ , with  $I(\theta)$  reaching a maximum or zero depending on whether  $2J_1(x)/x$  reaches its extremum or zero.

Diffraction effects limit the smallest diameter the Airy disc can take and therefore also the telescope's or imaging system's resolution. The angular size of the Airy disc is given by its radius from the centre of the disc (central maximum) out to the centre of the first dark interspace (inner, most conspicuous dark ring, the first minimum) between the central disc and the first bright diffraction ring (second maximum). Based on Airy diffraction theory, the Rayleigh criterion gives the theoretical resolution limit of a telescope, as determined by the radius of the Airy function's first null, and given by

$$\theta = 1.22 \frac{\lambda}{D} \quad (\text{radians}) = 206265 \left( 1.22 \frac{\lambda}{D} \right) \quad (\text{arc-seconds}), \quad (2.15)$$

where  $\theta$  is the angular resolution,  $\lambda$  the wavelength of incoming light and  $D$  the telescope aperture diameter. Point sources separated by an angle smaller than this angular resolution cannot be resolved. The factor of 1.22 is derived from calculating the position of the first dark ring surrounding the central Airy disc (Argyle, 2004; Napier-Munn, 2008). The diameter of the disc is directly proportional to the wavelength of the light but inversely proportional to the telescope aperture. The Airy disc diameter gets smaller for light of shorter wavelength (i.e. higher frequency) and in instruments of larger aperture. Therefore bigger telescopes produce better images of stars, i.e. smaller Airy discs. The smaller the Airy disc, the less it intrudes on detail. Poor seeing conditions make it appear as an amorphous blob. Although a telescope's theoretical angular resolution may be smaller than an arc-second, the telescope's resolving power will be limited further by adverse seeing conditions.

In order to determine the resolution limit of a telescope, close double stars may be observed to determine the smallest angular separation of double stars that can be observed by the telescope. Dawes' limit is applicable to the resolution of double stars and is based



on the observation of a pair of sixth magnitude stars. According to Dawes' limit, the resolving power of the telescope  $R$  is given by

$$R = \frac{11.6}{D} \text{ (arc-seconds)}, \quad (2.16)$$

where  $D$  is the aperture of the telescope in cm (Napier-Munn, 2008).

### 2.3.2. Fried parameter

The Fried parameter  $r_0$  is a statistical parameter derived from the Kolmogorov model of turbulence (Kolmogorov, 1941) by Fried (1965) and Fried (1966). The Fried parameter describes the effect of the atmosphere on the performance of a telescope and provides a measure of image degradation due to atmospheric turbulence. Variations in refractive index produce phase fluctuations of the wave front entering the telescope. The turbulent field is statistically described by a structure function and given by

$$D_\varphi(\rho) = \langle (\varphi_1 - \varphi_2)^2 \rangle, \quad (2.17)$$

where  $D_\varphi(\rho)$  is the atmospherically induced variance between the phase at two parts of the wave front,  $\varphi_1$  and  $\varphi_2$ , separated by a distance  $\rho$  in the aperture plane, and the triangle brackets denote ensemble averages. From this follows the phase structure function at the telescope aperture, given by

$$D_\varphi(\rho) = 6.88 \left( \frac{|\rho|}{r_0} \right)^{5/3}, \quad (2.18)$$

where the coherence length  $r_0$  (the Fried parameter) corresponds to the diameter of the telescope for which the resolution is beginning to be significantly affected by phase fluctuations (Tubbs, 2003). For telescopes with diameters larger than the Fried parameter, the resolution is no longer just limited by diffraction effects, but is also now seeing-limited. The resolution cannot be increased any further by increase of telescope aperture size (Travouillon, 2004).

Seeing can also be determined by measuring the smallest resolvable angular resolution of an object outside of Earth's atmosphere. Astronomers generally quantify the quality of optical seeing conditions at a particular site with a parameter they refer to as the "seeing".

Seeing  $\varepsilon_{FWHM}$  is described in terms of the Full Width at Half Maximum (FWHM) of the star's intensity profile, the Point Spread Function (PSF), at the focus of a telescope (Travouillon, 2004). Seeing  $\varepsilon_{FWHM}$  is related to the Fried parameter  $r_0$  by (Dierickx, 1992)

$$\varepsilon_{FWHM} = 0.98 \frac{\lambda}{r_0} \quad (\text{radians}) = 206265 \left( 0.98 \frac{\lambda}{r_0} \right) \quad (\text{arc-seconds}), \quad (2.19)$$

where  $\lambda$  is the wavelength of observation.

A larger  $r_0$  (therefore smaller  $\varepsilon_{FWHM}$ ) indicates better seeing conditions. The Fried parameter  $r_0$  typically takes on values of between 2 and 30 cm in the visible light range. This translates to seeing  $\varepsilon_{FWHM}$  values between 5.7" and 0.4", respectively, for  $\lambda = 550 \text{ nm}$ . The seeing is typically about one arc-second or less for a good astronomical site. The seeing quality of a site will vary with time and for different seasons (Travouillon, 2004).

## 2.4. Link between atmospheric turbulence and astronomical seeing

In summary of what has been discussed in the preceding sections, in the PBL of the troposphere, atmospheric turbulence is caused by wind and temperature gradients which cause refractive index variations. The refractive index variations distort electromagnetic wave fronts resulting in image degradation.

The vertical distribution of turbulence, as given by the profile of the refractive index structure parameter  $C_N^2(h)$ , allows for predicting atmospheric optical quality in terms of astronomical seeing. The integrated value of the index of refraction structure parameter for all atmospheric layers gives the total effect of the atmospheric turbulence and may be obtained by making use of the integral of Equation (2.13) and by measuring the atmosphere's temperature profile  $C_T^2(h)$  as well as the meteorological parameters, pressure  $P$  [hPa] and absolute temperature,  $T$  [K].

The Fried parameter  $r_0$  may be determined from the  $C_N^2(h)$  profile by (Roddier, 1981)

$$r_0(\lambda, \gamma, h) = \left( 16.7 \lambda^{-2} \frac{1}{\cos \gamma} \int_0^{\infty} C_N^2(h) dh \right)^{-3/5}, \quad (2.20)$$

where the turbulence strength  $C_N^2(h)$  varies as function of height  $h$  above the telescope,  $\gamma$  is the angle relative to zenith and  $\lambda$  the wavelength of light. Usually  $\gamma$  is chosen at zenith with  $1/\cos \gamma = 1$ .

Therefore, the expression for seeing, Equation (2.19), becomes (Vernin and Muñoz-Tuñón, 1992)

$$\varepsilon_{FWHM} = 0.98 \frac{\lambda}{r_0} = 5.25 \lambda^{-1/5} \left( \int_0^{\infty} C_N^2(h) dh \right)^{-3/5}, \quad (2.21)$$

and, knowing the wavelength of observation  $\lambda$  and height above the telescope  $h$ , the integrated value of the seeing  $\varepsilon_{FWHM}$  can be determined for a site. The inclusion of a turbulence-resolving model to obtain  $C_N^2(h)$  profiles for a specific site also allows one to estimate seeing at the site.

## **3. Methodology**

### **3.1. Introduction**

In this chapter, boundary layer numerical modelling with a Large Eddy Simulation (LES) model named the Large Eddy Simulation NERSC (Nansen Environmental and Remote Sensing Center) Improved Code (LESNIC), a turbulence-resolving simulation code developed by Igor Esau (Esau, 2004) at G.C. Rieber Climate Institute at the Nansen Environmental and Remote Sensing Center, is discussed. Methodology employed to obtain astronomical seeing from this turbulence-resolving model and its DATABASE64, a collection of LESNIC runs, is explained in detail.

An optical method to measure astronomical seeing is also implemented. It is explained how seeing may be quantified experimentally by comparison of an ideal and observe image. For the seeing monitor to be able to measure sub-arcsecond seeing conditions, it must itself have a resolution of better than an arc-second. Factors such as image scale and sampling, which determine the resolution the seeing monitor is capable of, are specified. The experimental method pertaining to image capture, stacking and evaluation as well as the measurement of double star separations is outlined.

### **3.2. Modelling seeing by turbulence method**

Atmospheric boundary-layer structure and behaviour may be simulated with numerical modelling (Garratt, 1992). With this approach, the PBL's dynamics, thermodynamics and interaction with the underlying surface are described by a set of differential equations, the Reynolds-averaged Navier-Stokes equations, and appropriate boundary conditions from fluid mechanics. Solutions of the equations are found by appropriate numerical methods. The volume occupied by the fluid is divided into a mesh. The governing equations with specified boundary and initial conditions are then solved for the mesh by applying a suitable algorithm.

Numerical models for solving the Navier-Stokes equations include Direct Numerical Simulation (DNS), Reynolds-Averaged Navier-Stokes (RANS) and Large Eddy Simulation (LES) (Pope, 2000). With LES, a more refined mesh than with RANS but a coarser mesh than with DNS is used. Solving the Navier-Stokes equations by DNS allows for the wide range of length and time scales associated with turbulent eddies to be resolved, but currently no computer exists with enough memory and speed to model configurations of the real PBL. By simply modelling the turbulent motions, as in the RANS approach, computational effort is reduced but depends heavily on the closure assumptions and does not provide finer PBL structure statistics. With LES, large eddies are resolved directly, while small eddies are filtered and modelled.

### **3.2.1. Large Eddy Simulation (LES)**

According to Stull (1988), Garratt (1992) and Pope (2000), LES is based on the Kolmogorov model of turbulence, a statistical analysis of turbulence (Kolmogorov, 1941 and Tatarski, 1961). In the LES approach, local unstable air masses called eddies are either resolved or modelled (Figure 3.1). Large-scale eddies are resolved directly while small-scale eddies are filtered out and modelled. By numerically filtering out the smaller eddies, which cannot be resolved explicitly, equations that govern the dynamics of large eddies only can be determined

Large-scale eddies are transporters of momentum, mass, energy and other passive scalars and are more problem-dependent than small-scale eddies. Large-scale eddies are therefore resolved through solving filtered partial differential equations governing turbulent fluid flow – the Navier-Stokes equations.

Small-scale eddies dissipate their energy through viscous interactions and are less dependent on the flow geometry. They are more isotropic than the larger scale eddies and therefore more universal, increasing the chances of finding a universal model. The small-scale eddies are therefore filtered out numerically and modelled. A filter width or grid spacing is employed in computations to filter out these eddies of smaller scale. These sub-

grid scale eddies' effect on the flow is then parameterised and may be modelled with a universal subgrid-scale model.

If realistic fields are to be derived for wind, temperature, humidity and pressure, factors such as turbulence, atmospheric composition, radiation, clouds, gravity waves, Earth's rotation, orography and surface friction should be considered when providing numerical solutions to the equations.

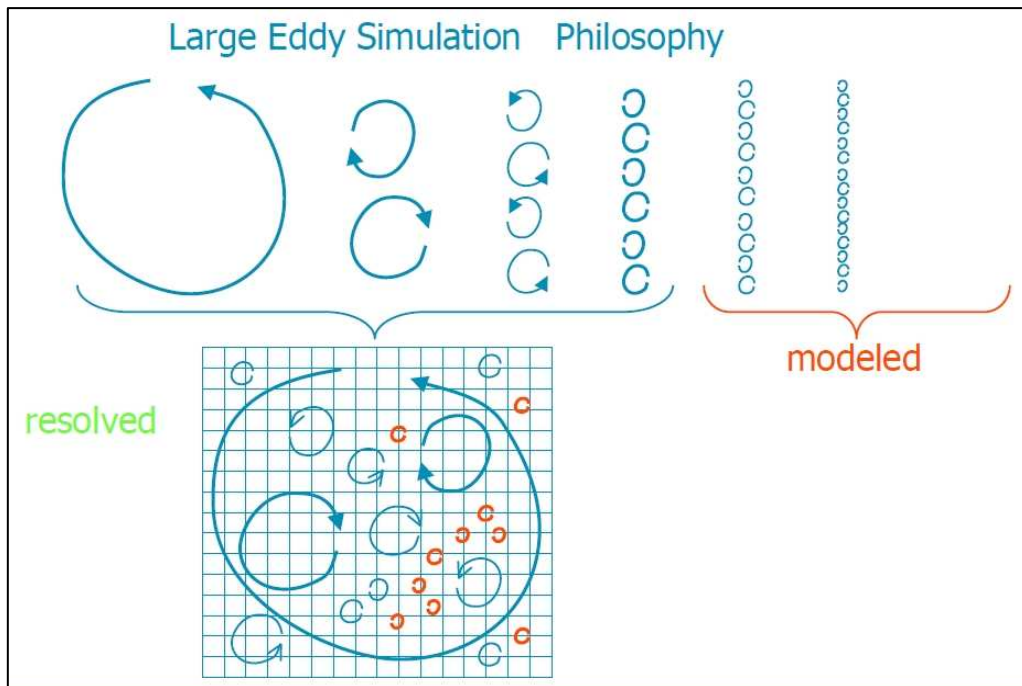


Figure 3.1. Large Eddy Simulation (LES) – large eddies are solved for while small eddies are filtered out and modelled (source: Harm Jonker, Delft University of Technology).

### 3.2.2. The LES NERSC Improved Code (LESNIC) and DATABASE64

Atmospheric turbulence is simulated by numerical modelling by making use of a turbulence-resolving simulation code called LESNIC (Esau, 2004) (Figure 3.2). It numerically solves the filtered Navier-Stokes equations of motions for incompressible Boussinesq fluid and the transport equations for the potential temperature and passive scalars. The LESNIC code has been used to compile a database of turbulence-resolving simulations, referred to as DATABASE64 (DB64) (Esau, 2004).

This database DB64 consists of a collection of LESNIC runs for a stably stratified planetary boundary layer (SBL) over a homogeneous aerodynamically rough surface (Esau, 2004). The runs simulate a period of 16 hours of PBL turbulence and produce three-dimensional fields of fluctuations of the potential temperature as well as three Cartesian components of the wind velocity,  $u$ ,  $v$  and  $w$ . Turbulence statistics and horizontally time-averaged profiles of required quantities are obtained by further processing of the above mentioned fluctuations.

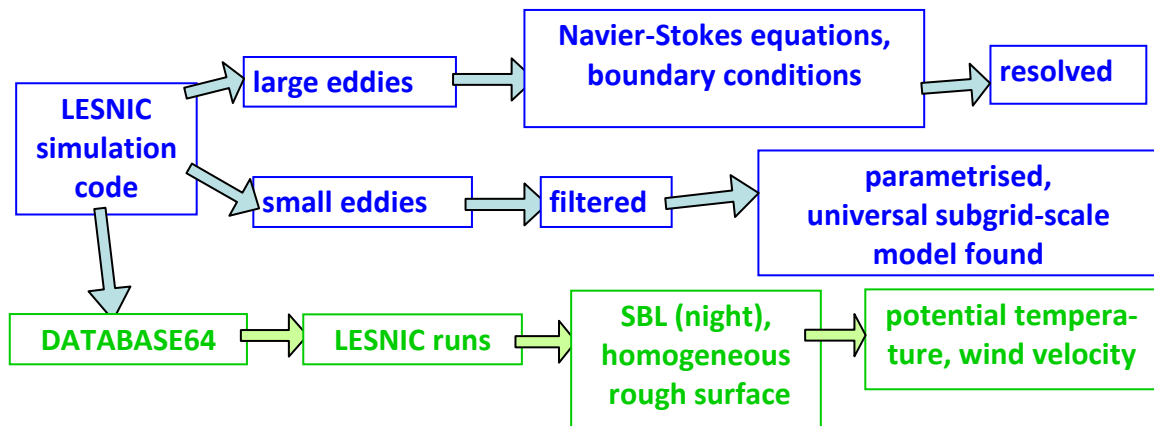


Figure 3.2. The LES NERSC Improved Code (LESNIC) provides a database of turbulence-resolving simulations, called DATABASE64.

### 3.2.3. Turbulence method – LESNIC modelling

Vertical profiles of  $C_N^2(h)$  as well as the Fried parameter  $r_0$  and seeing  $\epsilon_{FWHM}$  were obtained by using LESNIC runs from DATABASE64 for a stably stratified planetary boundary layer (SBL) over a homogeneous aerodynamically rough surface. The LESNIC runs are controlled by external parameters. Control parameters which vary from run to run for the first 8 LES runs are the following:

- the physical size of the domain range between 100 and 500 m in each of the x, y and z directions;
- the model is run for 45, 70 or 90 degrees latitude;
- the surface roughness for momentum takes on one of the values: 0.03, 0.05, 0.07 or 0.1 m;
- surface heat flux takes on one of the values: -2, -3, -4, -5 or  $-6 \times 10^{-3} \text{ K.m.s}^{-1}$ ;

- the Courant-Fridrihs-Levi (CFL) parameter used in calculating the time step is either 2.2 or 2.6.

The geostrophic wind was assigned a value of 3 or 5 m.s<sup>-1</sup> as an initial value. There are 64 grid levels between 0 and 200 m. A temperature of 10 °C (= 283 K), pressure of 90500 mbar (= 905 hPa = 90500 Pa) and relative humidity of 70% were assigned to all runs.

### $C_N^2(h)$ profiles

Profiles of  $C_N^2(h)$  were obtained by making use of Equation (2.13) and data from the LESNIC DATABASE64. An Octave program (see Appendix A2) was written and used to calculate  $C_N^2(h)$  from the  $C_T^2(h)$  profile as well as temperature  $T(h)$  and pressure  $P(h)$  profiles as follows (Figure 3.3):

- The  $C_T^2$  parameter was determined from rates of temperature variance dissipation  $\epsilon_\theta$  and turbulence kinetic energy dissipation  $\epsilon^{-1/3}$  in accordance with (André et al., 1978)

$$C_T^2 = 1.6 \epsilon_\theta \epsilon^{-1/3}, \quad (3.1)$$

where  $\epsilon_\theta$  and  $\epsilon^{-1/3}$  were provided by DATABASE64 for the specific run.

- Temperature  $T(h)$  and pressure  $P(h)$  profiles were determined by employing iteration to give

$$T_k(z_k) = T_{k-1} + \left( \left. \frac{d\theta}{dz} \right|_{z_{k-1}} + \gamma_{k-1} \right) \Delta z \quad (3.2a)$$

and

$$P_k(z_k) = P_{k-1} + \Delta P(T_k, r_{k-1}) = P_{k-1} - g \Delta z \rho = P_{k-1} - g \Delta z \frac{P_{k-1}}{R_{sd} T_{k-1}}, \quad (3.2b)$$

where

- $g$ : gravitational acceleration = 9.8076 m.s<sup>-2</sup>;
- $\rho$ : air density =  $P_{k-1}/R_{sd}T_{k-1}$  [kg.m<sup>-3</sup>];
- $R_{sd}$ : specific gas constant of dry air = 287.052 J.kg<sup>-1</sup>.K<sup>-1</sup>.



- The gradient of the potential temperature  $d\theta/dz$  and difference in level height  $\Delta z$  were provided by DATABASE64.
- The saturated adiabatic lapse rate  $\gamma$  is given by

$$\gamma = \frac{g \times \left( 1 + \frac{H_v \times r}{R_{sd} \times T} \right)}{c_{pd} + \frac{H_v^2 \times r \times \varepsilon}{R_{sd} \times T^2}}, \quad (3.3a)$$

where

$H_v$ : latent heat of vaporisation of water =  $2.257 \times 10^6 \text{ J.kg}^{-1}$  ;

$c_{pd}$ : specific heat of dry air at constant pressure =  $1004 \text{ J.kg}^{-1}.\text{K}^{-1}$  ;

$\varepsilon$ : ratio of gas constants for dry air and water vapour = 0.622 ;

and where the actual mixing ratio  $r$ , which is the ratio of the mass of water vapour to the mass of dry air, was calculated from a provided relative humidity  $RH$  to give

$$r = \frac{RH}{100} \times x_s, \quad (3.3b)$$

with the saturation mixing ratio  $x_s$  given by

$$x_s = \frac{\varepsilon e_s}{P}, \quad (3.3c)$$

and the saturation vapour pressure  $e_s$  given by the Clausius-Clapeyron equation

$$e_s = 611 e^{\left[ \frac{\varepsilon H_v}{R_{sd}} \left( \frac{1}{273} - \frac{1}{T} \right) \right]}. \quad (3.3d)$$

- Surface temperature  $T_1$  and surface pressure  $P_1$  were obtained from the base temperature  $T_{base}$  (= 283 K) and base pressure  $P_{base}$  (= 90500 Pa) at the site as given by

$$P_1 = P_{base} \quad (3.4a)$$

and

$$T_1 = T_{base} - \frac{\theta_*}{\kappa} \left( \log \frac{z_2}{2z_0} - \psi \left( \frac{z_2}{L_s} \right) \right), \quad (3.4b)$$

where

$$\psi\left(\frac{z_2}{L_s}\right) = 1 - 2.5 \frac{z_2}{L_s}, \quad (3.4c)$$

and the following are given by DATABASE64:

surface temperature flux scale  $\theta_*$ ;

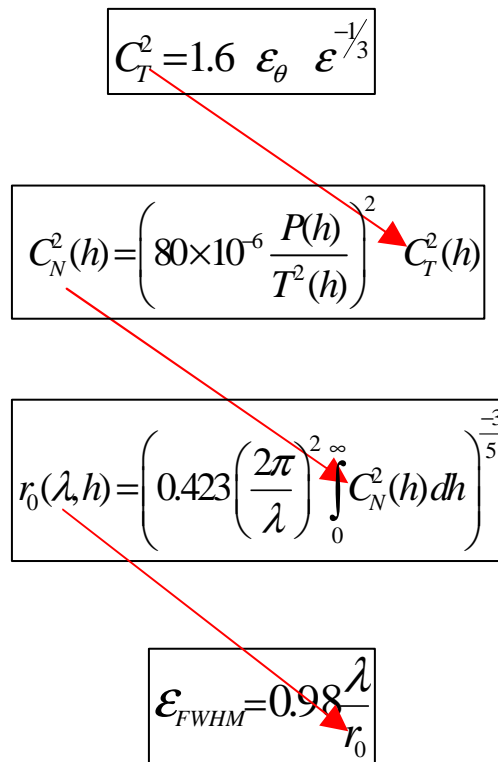
Von Karman constant  $\kappa = 0.4$ ;

surface roughness length scale  $z_0$ ;

and Monin-Obukhov length scale  $L_s$ .

### Seeing parameter values

The Kolmogorov model of turbulence provides a statistical parameter (Fried parameter  $r_0$ ) to characterise the seeing. The Fried parameter was obtained from Equation (2.20) by integrating  $C_N^2(h)$  with respect to zenith. Seeing, as given by  $\mathcal{E}_{FWHM}$ , is related to the Fried parameter by Equation (2.19) and is therefore given by Equation (2.21) (Figure 3.3). A turbulence-resolving model is able to produce  $C_N^2(h)$  profiles which may then be used to determine seeing at a site.



$$C_T^2 = 1.6 \varepsilon_\theta \varepsilon^{-1/3}$$

$$C_N^2(h) = \left( 80 \times 10^{-6} \frac{P(h)}{T^2(h)} \right)^2 C_T^2(h)$$

$$r_0(\lambda, h) = \left( 0.423 \left( \frac{2\pi}{\lambda} \right)^2 \int_0^\infty C_N^2(h) dh \right)^{-3/5}$$

$$\mathcal{E}_{FWHM} = 0.98 \frac{\lambda}{r_0}$$

Figure 3.3. Seeing from  $\varepsilon_\theta$ ,  $\varepsilon^{-1/3}$ ,  $P$  and  $T$  from DATABASE64.

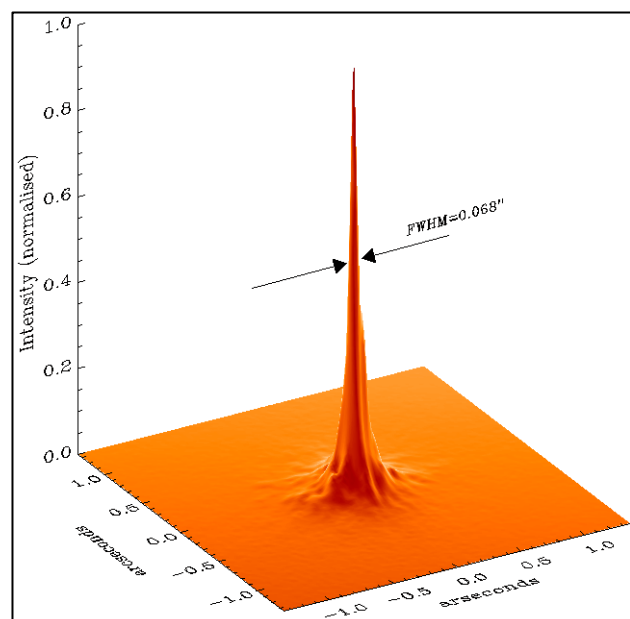
### 3.3. Measuring seeing by optical method

Seeing may be quantified experimentally by comparison of ideal and observed images. Ideally, the response of an imaging system to incoming radiation from a point source would be described by the theoretical Airy function (Equation (2.14)) (Longair, 1992; Roggeman and Welsh, 1996 and Tubbs, 2003). In reality, however, the Airy function is broadened by poor seeing conditions and the response of the imaging system is described by the Point Spread Function (PSF). Seeing conditions captured by an optical seeing monitor setup can be measured by comparing the observed PSF with the theoretical Airy function. The optimal telescope and Charge-Coupled Device (CCD) camera combination to be used in a seeing monitor setup is determined by the resolution required and therefore by factors such as image scale, telescope focal length, camera pixel size and shape.

#### 3.3.1. Point Spread Function (PSF)

Under ideal conditions, with no atmosphere present, the image of a point source is limited by diffraction effects only and is described by the theoretical Airy function (Equation (2.14)) (Longair, 1992 and Roggeman & Welsh, 1996). In reality, when imaging a point source, such as a star, the resulting image will not be a point, but will have spread out. This is due, not only to diffraction effects, but also to degradations of the electromagnetic wave front by turbulence in the atmosphere. Atmospheric turbulence distorts the image, and the distortions average out as a filled disc, called the PSF or seeing disc (Figure 3.4).

Figure 3.4. Example of a star's intensity profile or Point Spread Function (PSF) (source: Andrei Tokovinin, Cerro Tololo Inter-American Observatory (CTIO), Chile).



The PSF is used to characterise the imaging and provides the overall shape of the distribution of light which originates from a point source. It depicts where photons from a star have fallen, with the highest number of photons, the peak value, being accumulated in the central pixel in the profile. Aberrations and image motion broaden the PSF.

### 3.3.2. Image scale

The image scale gives the amount of sky covered by a single pixel of the CCD camera. It is dependent on the CCD camera's pixel size and the focal length of the telescope. The focal length of the telescope is the distance from the primary mirror or lens to the focal point where the light rays converge. Image scale is measured in arc-seconds per pixel according to the formula (Wodaski, 2002)

$$\text{Image scale} = \frac{205 \times \text{CCD pixel size } (\mu\text{m})}{\text{telescope focal length } (\text{mm})} \quad (3.5)$$

Smaller pixel size and longer focal length give higher resolution images.

### 3.3.3. Sampling

Sampling refers to the number of pixels that a star image covers. If the image covers too few pixels, it is an under sampled image and the best possible resolution is not achieved. Critical sampling may be determined from the width of the PSF. For a Gaussian PSF, with the resolution measured across the diagonal of a square pixel, this corresponds to a critical sampling frequency of (Howell, 2006)

$$FWHM = \sqrt{2} \times 2.355 = 3.33 \text{ pixels} , \quad (3.6a)$$

where  $FWHM$  is the full-width at half-maximum of the PSF (Figure 3.5).  $FWHM$  is the diameter at which the star's intensity distribution falls to one-half of its peak value.

In order to obtain the required resolution of 1 arc-sec an image scale of less than

$$\frac{1 \text{ arc-sec}}{3.33 \text{ pixels}} = 0.3 \text{ arc-sec per pixel} \quad (3.6b)$$

is required.

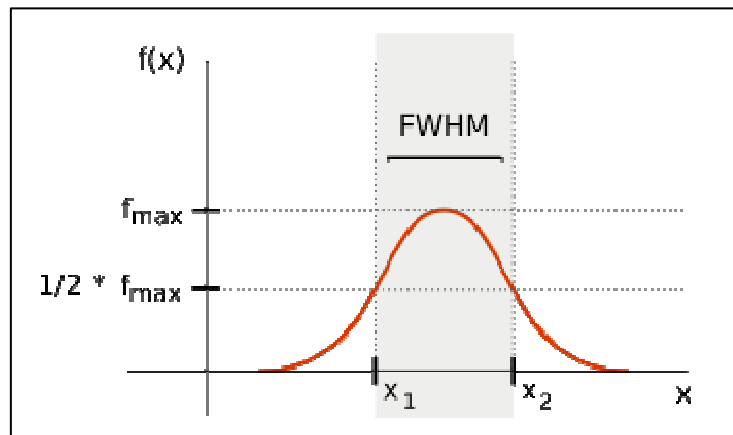


Figure 3.5. Full Width at Half Maximum (FWHM) of a Gaussian distribution (source: Arne Nordmann, Wikipedia).

### 3.3.4. Experimental method

Images captured by CCD were statistically analysed and compared with the theoretical Airy function, which is a measure of an absence of turbulence (Figure 3.6). Deviation from the Airy function gives an indication of seeing conditions. Close double stars were also observed for calibration and verification purposes.

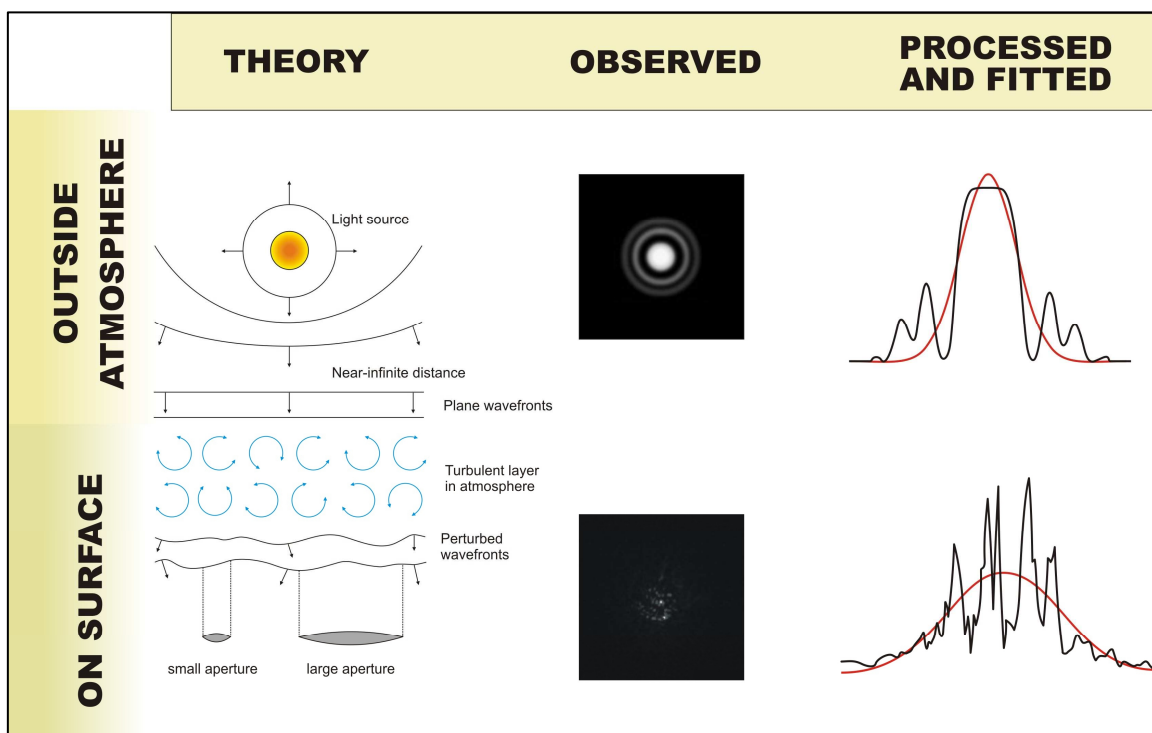


Figure 3.6. Diagrammatic representation of seeing analysis process (courtesy: Roelf Botha).

## Image capture

Seeing varies spatially as well as temporally (Erasmus, 1986; Erasmus 2000 and Roddier, 1981). Seeing varies with elevation angle and is best at zenith. Seeing also changes with season, from night to night, with time of night and at a rate of more than 100 Hz. Usual terrain layouts are non-uniform and therefore have an influence on turbulence generation; seeing will be different for different classes of terrain.

Taking all this into account, we can deduce that for a site:

- stars at various positions on the night sky must be observed;
- observations must be made at different times;
- long-term data collection is required and
- observations must be made from various on-site locations.

Numerous short exposure images of a specific source were captured to allow for sampling of seeing variations and short-term image wander. Short exposure times eliminate telescope tracking errors (which contribute to image width) and allow for the “freezing” of atmospheric turbulence. Exposure times of 3 or 4 seconds allow for sampling of seeing variations and short-term image wander but are not influenced by bad tracking.

## Image stacking and evaluation

The images were evaluated individually but could also be stacked to obtain an average output image of the star’s intensity distribution, the PSF. Stacking was not implemented in this work. The PSF is broadened by poor seeing conditions (Longair, 1992; Roggeman and Welsh, 1996 and Tubbs, 2003). The broadened PSF was compared with the theoretical Airy function. A quantitative measure of the seeing was obtained by fitting an appropriate function, a bell-shaped Gaussian intensity profile, to the PSF (Roddier, 1981) and determining the Gaussian profile’s FWHM value.

The FWHM of a star’s intensity distribution at the focus of the telescope describes the seeing  $\epsilon_{FWHM}$ . This is related to the standard deviation from the Gaussian distribution  $\sigma$  by (Wargau, 1994)

$$\epsilon_{FWHM} = FWHM = 2\sqrt{2 \ln 2} \sigma \approx 2.355 \sigma \quad (3.7a)$$

in seconds of arc (number of FWHM pixels multiplied by image scale in arc-seconds per pixel). The Fried parameter  $r_0$ , as given by Equation (2.19), may be obtained from seeing observations through the relation

$$\epsilon_{FWHM} \approx 2.355 \sigma = 206265 \left( 0.98 \frac{\lambda}{r_0} \right), \quad (3.7b)$$

where  $\lambda$  is the wavelength of observation.

### Measuring double star separation

Due to diffraction, the Airy disc represents the smallest point to which a light beam can be focused in accordance with the Rayleigh criterion of Equation (2.15). Similarly, the Dawes limit, as given by Equation (2.16), is applicable to resolving double stars, specifically a pair of white stars, each of magnitude 6 brightness (Napier-Munn, 2008). Dawes' limit represents the closest angular separation between two such stars with the stars still resolvable as separate objects, i.e. with the observer still being able to 'split the double'. If the two stars' Airy discs overlap, a single elongated star will be observed. If one star's Airy disc falls in the first dark diffraction ring of the other star, the two stars will be observed as two small disks forming a figure of eight (Figure 3.7).

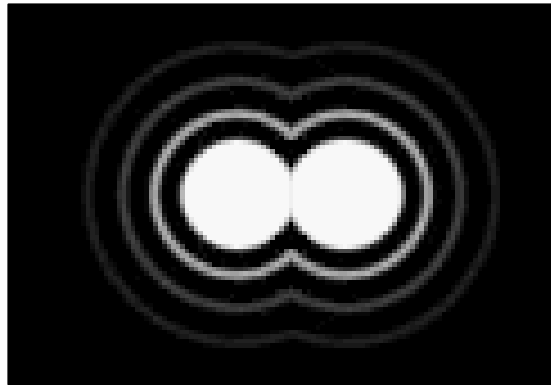


Figure 3.7. Binary stars: overlapping Airy discs (source: The Royal Astronomical Society of Canada, Calgary Centre).

Successively closer double stars will be observed until a limit is reached where a pair can no longer be resolved. The achieved resolution limit will be compared with the telescope's theoretical resolution limit (according to the Rayleigh criterion and Dawes' limit) in order to determine seeing conditions.

## **4. Seeing monitor – proposed design**

### **4.1. Introduction**

An investigation into suitable hardware components for the seeing monitor is detailed in this chapter. A possible seeing monitor setup is proposed. Astronomical seeing conditions conducive to the propagation of the LLR's laser beam are those for which the seeing is at better than arc-second resolution level. The seeing monitor setup must therefore be capable of a theoretical resolution of better than an arc-second not to be the limiting factor for image quality during astronomical seeing measurements. The proposed system is to consist of a telescope, CCD camera and control/processing PC. The seeing monitor's requirements with respect to the telescope mount, automation and infrastructure will also be discussed. Instrumentation that should be co-hosted on-site in support of seeing measurements with the seeing monitor setup, as well as in support of LESNIC modeling, are briefly mentioned (with a more thorough description of such instruments given in the Appendix A4).

### **4.2. Hardware requirements**

The optimal combination of telescope and CCD camera must deliver a theoretical resolution of better than 1 arc-second if it is to measure whether seeing below 1 arc-second is possible at a site. For an image not to be under sampled, a critical sampling frequency of 3.33 pixels is required according to Equation (3.6a), which means that the star image must cover at least 3.33 pixels of the CCD sensor. According to Equation (3.6b), to achieve a resolution of better than 1 arc-second and a critical sampling frequency of at least 3.33 pixels, an image scale of less than 0.3 arc-second per pixel is required. Equation (3.5) was used to compile the graph in Figure 4.1. The graph depicts the Field Of View (FOV) per pixel, i.e. the image scale, resulting from various telescope aperture and focal ratio sizes in combination with various CCD sensor pixel sizes. It can be deduced from this graph that the larger the telescope's aperture and the higher its focal ratio and the smaller the CCD sensor's pixel size, the better the resolution achieved.



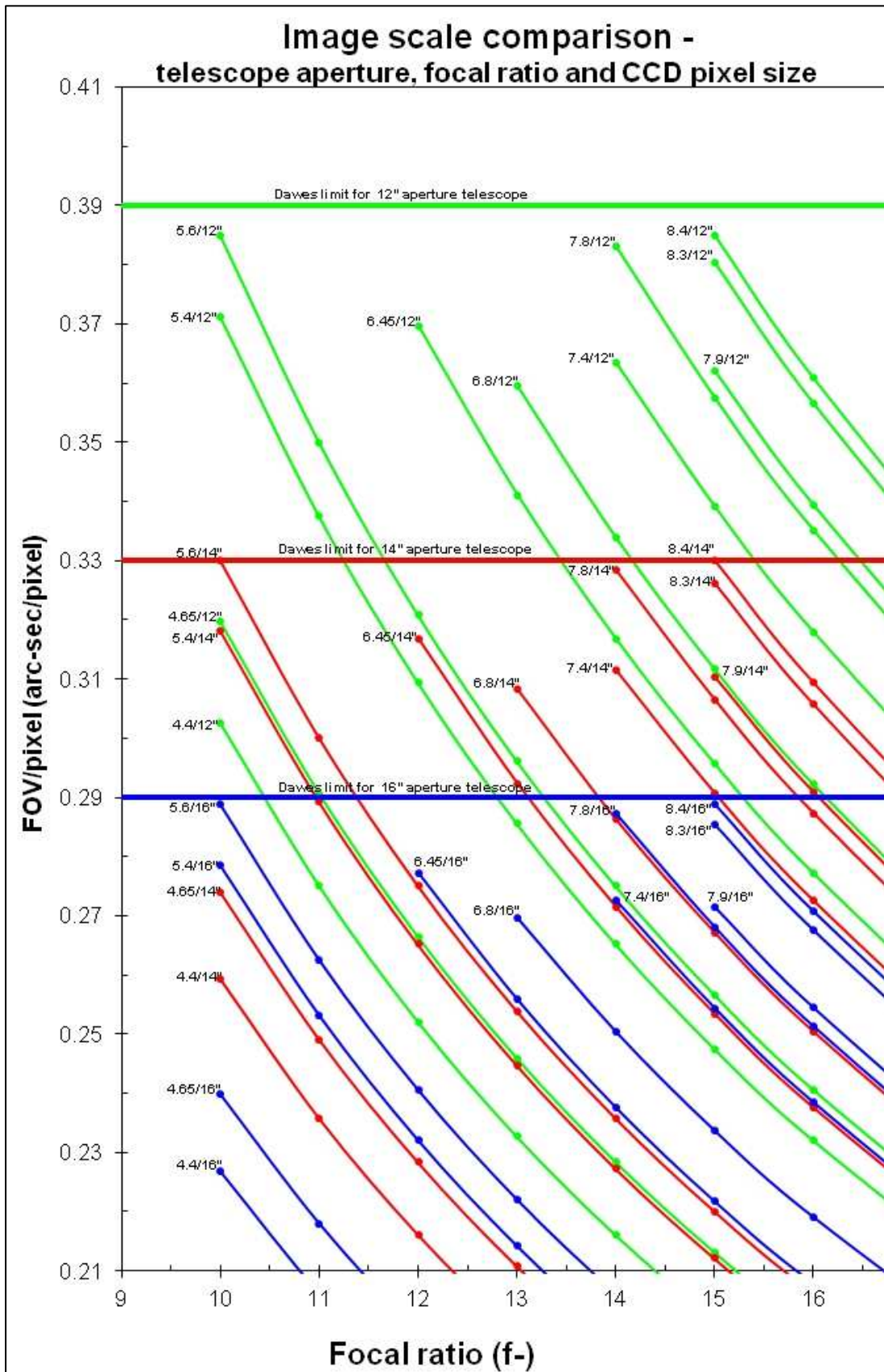


Figure 4.1. Graph depicting possible telescope and camera combinations.

CCD sensor pixel size will be chosen in accordance with a predetermined telescope diameter and focal length, with the combination comparable to Airy disc size to fully utilise the capabilities of the optics. A suitable mount, which is able to accommodate the weight and dimensions of the Optical Tube Assembly (OTA) of the telescope and all its attachments, in particular the CCD camera, must be found for the required imaging resolution to be achievable.

#### **4.2.1. Telescope**

The following discussion is based on information obtained from Mobberley (1998), Starizona (2000) and Wodaski (2002). According to Equation (3.5), the image scale depends on both the focal length of the telescope and the size of the pixels in the camera sensor. Long focal lengths and small pixels result in a smaller image scale and therefore higher resolution. The focal length of a telescope is given by

$$FL = D \times f\text{-ratio} , \quad (4.1)$$

where  $FL$  is the focal length in mm,  $D$  the aperture diameter in mm and the  $f\text{-ratio}$  is the focal ratio, which is a dimensionless quantity. For a given aperture diameter, the higher (longer, slower) the focal ratio the longer the focal length of the telescope and therefore the smaller the image scale for a specific CCD sensor pixel size.

Regarding the choice of the telescope OTA then, for the best resolution, the largest aperture telescope with the highest focal ratio is required. This was the primary requirement in choosing the most suitable telescope. Further requirements with regard to excellence of optical quality, GOTO functionality (for easy automation), sturdiness of the mount and portability of the setup were also considered.

#### **4.2.2. CCD camera**

The following discussion is based on information obtained from Martinez and Klotz (1998) as well as Howell (2006). A CCD camera is a detector which makes use of the photo-electric effect to convert incoming photons to electrons at photo-sensitive sites known as pixels. The electronic charge is transferred during readout. Voltage is converted to a digital

signal to produce a digitised image. Definitions of terms describing CCD camera characteristics are provided in Appendix A3.

In comparing various CCD camera models (in effect the CCD chips), although the primary consideration was to find an ideal match between CCD pixel size and telescope focal length, other CCD camera specifications that were also considered are as follows:

*Monochrome / colour* - due to higher sensitivity, a monochrome CCD camera is required.

*Number of pixels in array* - with relatively small pixel size, a large number of pixels in the pixel array is required to ensure a FOV wide enough to avoid difficulties with centring and focusing of the star image.

*Full frame / frame transfer / interline* - a full-frame CCD camera is preferred over frame transfer or interline CCD cameras, as sensitivity is compromised in the latter two types due to their mode of charge transfer and readout.

*Readout rate / frame rate / minimum exposure length* - to capture turbulence fluctuating at 100 - 200 Hz, high readout and maximum frame rates as well as the shortest possible minimum exposure length are required.

*Dimensions / weight* - the CCD camera's dimensions and weight should be as small as possible to allow for problem-free mount-clearance and as little weight as possible to be added to the payload.

*Interface / transfer rate* - computer connectivity should be established by means of a USB 2.0 or Firewire (IEEE1394) PC interface and high transfer rates are required.

*Digital resolution* - a digital resolution with at least 14-bit Analogue to Digital (A/D) conversion for full use of a high Dynamic Range (large Full-Well Capacity, low Read Noise) is required.

*Operating temperature* - the CCD camera should be able to operate at a range of temperatures from below 0 °C to above 30 °C with regulated cooling to reduce Dark Current.

*Power consumption* - low power consumption requirements are necessary as power will be supplied by battery charged by solar panel.

### **4.2.3. Mount**

The following discussion is based on information obtained from Mobberley (1998), Starizona (2000) and Wodaski (2002). For commercially available telescopes, the OTA and mount, together with the drive system, are oftentimes sold as a pre-assembled package. The mount is the determining factor for long focal-length, high-resolution astronomical imaging. A quality mount is required for CCD imaging. It must be sturdy enough to support a heavy load without any flexure and must be able to damp any vibrations quickly. The mount together with its drive motors must track accurately and any gearing must have very low backlash.

The two basic telescope mount designs are the alt-az and equatorial mounts. The SCTs sold with computerised alt-az fork mounts and German Equatorial Mounts (GEM) are popular for use in CCD imaging. These GOTO mounts have on-board computers for locating stars and commanding drive motors to point the telescope at and track these stars across the sky. The more stable the mount, the greater the pointing accuracy and tracking precision. To follow, a short summary of the strengths and weaknesses of these two types of mount:

#### **Fork mount**

Commercial fork mounts tend to be mechanically unstable. This type of mount also has limited space between the back of the telescope, where the CCD camera is attached, and the base of the fork. Large CCD cameras will therefore not be able to clear the base of the fork when the telescope is pointing at declinations near zenith. Fork-mounted telescopes can, however, cross the meridian without any problem. Variable-rate motors on both axes are controlled by computer and allow the telescope to track the desired star. Field rotation must be corrected for by the addition of a de-rotator. By attaching an equatorial wedge between the fork mount and telescope, the fork mount is transformed into an equatorial mount. Stars can then be tracked with a constant-speed motor on the polar axis and field rotation does not occur.

## **German Equatorial Mount (GEM)**

This type of mount has a short fulcrum and delivers the best mechanical stability. It is also capable of carrying more load than a fork mount and is easier to balance. The mount has two axes of rotation and can point a telescope anywhere in the sky. A motor turns the mount on the axis which is aligned with the celestial pole (Right Ascension, (RA)), which enables it to track at the sidereal rate. The Declination (Dec) axis moves at right angles to the RA axis. With a GEM, the CCD camera or even the telescope can strike the pier when crossing the meridian. A telescope with a GEM must therefore be flipped from the western to the eastern side of the mount before crossing the meridian. This will interrupt imaging and may affect accuracy during the remainder of the observing session.

## **4.3. Hardware selection**

### **4.3.1. Telescope**

The following discussion is based on information obtained from Mobberley (1998), Starizona (2000) and Wodaski (2002). To follow, a short description of the basic telescope optics used in the design of telescope Optical Tube Assemblies (OTAs):

- Refracting telescopes make use of an objective lens to bring the starlight to a focus at the back of the telescope.
- Prime focus reflecting telescopes make use of a paraboloidal primary mirror to reflect light back to a detector at prime focus.
- Newtonian reflecting telescopes consist of a paraboloidal primary mirror, which reflects starlight onto a flat secondary mirror, tilted at  $45^\circ$  to reflect the light onto the detector at the side of the telescope.
- Cassegrain reflecting telescopes use a paraboloidal primary mirror to reflect starlight onto a hyperboloidal secondary mirror, which then reflects the lights back through a hole in the centre of the primary mirror and out to the detector.

Different types of commercially available telescope OTA designs were compared (Table 4.1). The various designs all include the required large aperture diameter telescopes

Table 4.1. Comparison of commercially available telescope Optical Tube Assemblies (OTAs).

| Telescope design                   | Refractors  | Reflectors – Newtonian / Dobsonian   | Schmidt-Cassegrain (SCT)  | Maksutov-Cassegrain  | Classical Cassegrain       | Ritchey-Chrétien (RC)                     |
|------------------------------------|---|--|---|--|----------------------------|---|
| <b>Types</b>                       | Achromatic (AC)<br>Apochromatic (APO)                                 | Dobsonians (Dobs)<br>Schmidt-Newtonians (S-N)<br>Maksutov-Newtonian (M-N)                        |   |  |                            |   |
| <b>Aperture diameter</b>           | 2"-14"  | Dobs: 3"-17.5"<br>Newts: 3"-16"  | 3.5"-20"  | 4"-13"   | 10"-16"                    | 6"-23.6"                                  |
| <b>Focal length</b>                | 324-4272 mm   | Dobs: 300-2225 mm<br>Newts: 600-2436 mm  | 1034 - 4064 mm  | 1251- 4290 mm  | 3810- 6090 mm              | 1372- 4800 mm                             |
| <b>Focal ratio</b>                 | f/5-f/15  | Dobs: f/3.95-f/9<br>Newts: f/3.6-f/9.75  | f/8-f/13.8  | f/11.5-f/13.9  | f/12 – f/20                | f/5.4– f/9                                |
| <b>Aberrations</b>                 | AC: chromatic   | Coma<br>M-N: Maksutov corrector lens for coma<br>S-N: Schmidt corrector for spherical aberration | Schmidt corrector lens for spherical aberration; aspheric secondary mirror for coma | Maksutov corrector lens for spherical aberration; aspheric secondary mirror for coma | Coma<br>Field curvature    | Field correctors for residual astigmatism |
| <b>Optical quality</b>             | APO: excellent  | M-N: excellent   |   |  |                            | Very good                                 |
| <b>Imaging</b>                     | Short f-ratios popular for wide-field; large APOs for high-resolution |  | Wide-field & high-resolution  |  | Mostly high-resolution     | Mostly high-resolution                    |
| <b>OTA – dimensions and weight</b> | 280-2280 mm<br>0.38–100? kg   | Dobs: 457-2235 mm<br>1.8-59.88 kg<br>Newts: 400-2438 mm<br>1.6-50 kg                             | 279-1016 mm<br>2.1-87 kg  | 254-933 mm<br>1.4-19.8 kg  | 1016-1677 mm<br>18.2-59 kg | 457-1790 mm<br>5.9-115 kg                 |
| <b>Mounts</b>                      | Depends on OTA dimension, weight                                      | Depends on OTA dimensions, weight  | Small, computer-controlled  |  |                            |   |
| <b>Portability</b>                 | Less portable than SCTs of same aperture                              | Less portable than SCTs of same aperture   | Compact   | Compact  | Reasonably compact         | Compact                                   |

in their range. Newtonian/Dobsonian reflectors as well as Ritchey-Chrétien (RC) telescopes, however, do not meet the requirement of a high focal ratio. The seeing monitor requires a telescope that is compact and portable for field work. Large-aperture

Newtonian/Dobsonian reflectors and refractors are large and unwieldy instruments compared to Cassegrain telescopes of similar aperture and are not very portable. Classical Cassegrain telescopes have longer tubes than Schmidt-Cassegrain and Maksutov-Cassegrain telescopes of similar aperture. Maksutov-Cassegrain and classical Cassegrain telescopes with the required large apertures and high focal ratios are not readily available. The choice thus fell on the commercially available Schmidt-Cassegrain telescopes (SCTs).

Commercially available SCTs have focal ratios of  $f/10$ . These telescopes are popular for CCD imaging as they are versatile, providing for both high-resolution and wide-field imaging. Spherical aberration is minimised by employing a Schmidt corrector lens. Coma may be eliminated by employing an aspheric secondary mirror. A secondary mirror is employed to pack a longer focal length into a shorter tube. This folded optical design delivers a compact, light-weight telescope requiring a smaller mount, which adds to portability. Some of the commercially available SCTs include a computer-controlled mount with GOTO functionality. The telescope is easy to set up and use and provides easy access for a CCD camera. By the Dawes limit of Equation (2.16) and as indicated in Table 4.2, only telescopes with aperture diameters of 14" and above are capable of delivering a theoretical resolution of  $\sim 0.3$  arc-sec. A second-hand 14" Meade LX200 GPS SCT with a computer-controlled heavy-duty altitude azimuth (alt-az) fork-type mount was purchased (Figure 4.2).



Figure 4.2. Recently acquired second-hand 14" Meade LX200 GPS SCT with alt-az fork-arm mount and field tripod.

### 4.3.2. CCD camera

The commercially available SCTs have relatively short focal ratios of  $f/10$ . Although the focal length of a telescope may be increased by inserting a Barlow lens into the optical path, this would just add another optical component to the light path and flaws may be magnified. It would be preferable to match aperture diameter and  $f$ -ratio (in other words focal length, see Equation (3.5) and Equation (4.1)) with CCD pixel size to deliver the required FOV of  $\sim 0.3$  arc-sec per pixel (in accordance with Equation (3.6b)). A focal ratio of  $f/10$  and aperture diameter of 14" therefore limited possible combinations to those with CCD cameras with sensor pixel sizes of 4.4, 4.65, 5.4 or 5.5  $\mu\text{m}$  at most. Popular commercially available CCD cameras in this pixel-size range are listed in Table 4.2.

Table 4.2. Dawes' limit (red) for specific telescope aperture sizes and FOV/pixel for various CCD camera / telescope aperture combinations. Focal ratio of telescope under consideration is  $f/10$  in all cases.

| CCD camera                                     | Pixel size<br>[square sides]<br>$\mu\text{m}$ | # Pixels |      | Telescope aperture ( $f/10$ ) |             |             |             |             |
|--|---|----------|------|-------------------------------|-------------|-------------|-------------|-------------|
|  |   |          |      | 25 cm                         | 27.5 cm     | 30 cm       | 35 cm       | 40 cm       |
|  |   |          |      | 10"                           | 11"         | 12"         | 14"         | 16"         |
| <b>Dawes' limit = <math>11.6/D</math> (cm)</b> |   |          |      | <b>0.46</b>                   | <b>0.41</b> | <b>0.38</b> | <b>0.32</b> | <b>0.28</b> |
|  |   |          |      | FOV/pixel (arc-sec/pixel)     |             |             |             |             |
| Point Grey GRAS-20S4M                          | 4.4   | 1624     | 1224 | 0.36                          | 0.30        | 0.30        | 0.26        | 0.23        |
| ATIK 320E                                      | 4.4   | 1620     | 1220 | 0.36                          | 0.30        | 0.30        | 0.26        | 0.23        |
| IS DMK 51                                      | 4.4   | 1600     | 1200 | 0.36                          | 0.30        | 0.30        | 0.26        | 0.23        |
| Lumenera SKYnyx2-2                             | 4.4   | 1616     | 1232 | 0.36                          | 0.30        | 0.30        | 0.26        | 0.23        |
| Apogee Ascent A205                             | 4.65  | 1360     | 1024 | 0.38                          | 0.35        | 0.32        | 0.27        | 0.24        |
| ATIK 314E                                      | 4.65  | 1360     | 1024 | 0.38                          | 0.35        | 0.32        | 0.27        | 0.24        |
| FLI MLx205                                     | 4.65  | 1360     | 1024 | 0.38                          | 0.35        | 0.32        | 0.27        | 0.24        |
| IS DMK 41                                      | 4.65  | 1280     | 960  | 0.38                          | 0.35        | 0.32        | 0.27        | 0.24        |
| Lumenera SKYnyx2-1                             | 4.65  | 1392     | 1040 | 0.38                          | 0.35        | 0.32        | 0.27        | 0.24        |
| IS DMK 31                                      | 4.65  | 1024     | 768  | 0.38                          | 0.35        | 0.32        | 0.27        | 0.24        |
| Apogee Alta U8300                              | 5.4   | 3326     | 2504 | 0.45                          | 0.41        | 0.37        | 0.32        | 0.28        |
| ATIK 383L+                                     | 5.4   | 3326     | 2504 | 0.45                          | 0.41        | 0.37        | 0.32        | 0.28        |
| FLI ML8300M                                    | 5.4   | 3326     | 2504 | 0.45                          | 0.41        | 0.37        | 0.32        | 0.28        |
| Orion Parsec 8300M                             | 5.4   | 3326     | 2504 | 0.45                          | 0.41        | 0.37        | 0.32        | 0.28        |
| QSI 5/683S                                     | 5.4   | 3326     | 2504 | 0.45                          | 0.41        | 0.37        | 0.32        | 0.28        |
| SBIG ST/STF8300M                               | 5.4   | 3326     | 2504 | 0.45                          | 0.41        | 0.37        | 0.32        | 0.28        |
| Apogee Ascent A1050                            | 5.5   | 1024     | 1024 | 0.45                          | 0.41        | 0.37        | 0.32        | 0.28        |
| FLI ML01050                                    | 5.5   | 1024     | 1024 | 0.45                          | 0.41        | 0.37        | 0.32        | 0.28        |
| Apogee Ascent A2050                            | 5.5   | 1600     | 1200 | 0.45                          | 0.41        | 0.37        | 0.32        | 0.28        |
| Apogee Ascent A2150                            | 5.5   | 1920     | 1020 | 0.45                          | 0.41        | 0.37        | 0.32        | 0.28        |
| Apogee Ascent A4050                            | 5.5   | 2336     | 1752 | 0.45                          | 0.41        | 0.37        | 0.32        | 0.28        |
| Apogee Ascent A8050                            | 5.5   | 3296     | 2472 | 0.45                          | 0.41        | 0.37        | 0.32        | 0.28        |
| FLI ML8050                                     | 5.5   | 3296     | 2472 | 0.45                          | 0.41        | 0.37        | 0.32        | 0.28        |
| Apogee Acent A29050                            | 5.5   | 6576     | 4384 | 0.45                          | 0.41        | 0.37        | 0.32        | 0.28        |
| FLI ML29050                                    | 5.5   | 6600     | 4408 | 0.45                          | 0.41        | 0.37        | 0.32        | 0.28        |
| Point Grey GRAS-03K2M                          | 7.4   | 640      | 480  | 0.61                          | 0.55        | 0.51        | 0.43        | 0.38        |



In Table 4.3, CCD cameras in the 4.4- to 5.5- $\mu\text{m}$  range (listed in Table 4.2) were compared with respect to the specifications referred to in Section 4.2.2.

Table 4.3. Comparison of CCD cameras appearing in Table 4.2 according to the specifications discussed.

| CCD camera   | Advantages   | Disadvantages  |
|--|--|--|
| Apogee Ascent<br><br>Apogee Alta   | Some models - large number of pixels in array...<br>Some models - high frame rate<br>16-bit ADC<br>OS: W/L/M<br><br>KAF-8300 FF chip with mechanical shutter<br>Large number of pixels in array<br>16-bit ADC<br>Large FWC                                   | ... but slow frame rates<br>Expensive to very expensive<br>CCD type: IL<br>Large body<br><br>Expensive<br>Min $t_{\text{exp}} = 30$ ms<br>Large, heavy body<br>Max $T_{\text{op}} = 27$ °C |
| ATIK 320E & 314E<br><br>ATIK 383L+   | 16-bit ADC<br>Light in weight<br><br>KAF-8300 FF chip with mechanical shutter<br>Large number of pixels in array<br>16-bit ADC<br>Large FWC  | CCD type: IL<br>Large body<br><br>Min $t_{\text{exp}} = 200$ ms<br>Large body<br>High power requirements   |
| FLI<br><br>FLI ML8300M   | Some models - large number of pixels in array...<br>16-bit ADC<br>Most models - wide range of $T_{\text{op}}$<br><br>KAF-8300 FF chip with mechanical shutter<br>Large number of pixels in array<br>16-bit ADC<br>Wide range of $T_{\text{op}}$<br>Large FWC | ... and slow frame rates<br>Very expensive<br>CCD type: IL<br><br>Expensive<br>Min $t_{\text{exp}} > 6$ ms<br>Large body   |
| IS DMK   | Inexpensive<br>Some models - high frame rate ...<br>Small, light body<br>USB 2.0 / Firewire / GigE<br>Max $T_{\text{op}} = 45$ °C<br>Low power requirements  | CCD type: IL<br>... but small number of pixels in array<br>8-bit ADC<br>Min $T_{\text{op}} = -5$ °C<br>Min $t_{\text{exp}} > 6$ ms   |
| Lumenera SKYnyx  | Light body<br>Max $T_{\text{op}} = 50$ °C<br>Low power requirements  | Expensive<br>Low frame rate<br>8- & 12-bit ADC   |
| Orion Parsec 8300M   | KAF-8300 FF chip with mechanical shutter<br>Large number of pixels in array<br>16-bit ADC<br>Large FWC   | Min $t_{\text{exp}} = 6$ ms<br>Heavy body<br>High power requirements   |
| QSI 5/683S   | KAF-8300 FF chip with mechanical shutter<br>Large number of pixels in array<br>16-bit ADC<br>Large FWC<br>Min $T_{\text{op}} = -20$ °C<br>OS: W/L/M  | Expensive<br>Min $t_{\text{exp}} = 30$ ms<br>Large, heavy body<br>Max $T_{\text{op}} = 30$ °C<br>High power requirements   |
| Point Grey GRAS-20S4M<br>(for PSF seeing monitor)  | Min $t_{\text{exp}} = 0.02$ ms<br>Small, light body<br>Firewire<br>Max $T_{\text{op}} = 40$ °C<br>Low power requirements<br>OS: L/M  | CCD type: IL<br>Min $T_{\text{op}} = 0$ °C   |
| SBIG ST/STF8300M   | KAF-8300 FF chip with mechanical shutter<br>Large number of pixels in array<br>16-bit ADC<br>Large FWC<br>OS: W/L/M  | Min $t_{\text{exp}} = 100$ ms<br>Large, heavy body<br>High power requirements  |
| IL=Interline; FOV=Field Of View; $T_{\text{op}}$ =operating Temperature ; ADC=Analogue-to-Digital Conversion; OS=Operating System;<br>W=Windows; L=Linux; M=Mac; FWC=Full-Well Capacity; FF=Full-Frame; $t_{\text{exp}}$ = exposure time |  |  |

The initial decision was to select from CCD cameras containing the Kodak KAF-8300 chip (5.4- $\mu\text{m}$  pixel size, see Table 4.2). From the initial selection appearing in Table 4.2, these cameras are the only full-frame CCD cameras with mechanical shutters. The decision changed once Tim Pickering of SAAO placed the software of the DIMM component of their SALT MASS-DIMM at our disposal. Setting up a DIMM configuration would simply equate to placing a two-hole mask at the telescope’s entrance aperture, a prism at one of the two small sub-apertures, and a high-speed CCD camera at the back of the telescope. The SALT DIMM software, TimDIMM, supports an IEEE1394 Firewire CCD camera, the Point Grey Grasshopper GRAS-03K2M (highlighted in blue at the bottom of Table 4.2) and runs on a Mac mini under OS X. The TimDIMM software could also be adapted to run under Linux but would require the IEEE1394 interface to be in at an added expense, while this interface is already built into the Mac mini. It was therefore decided to acquire the Point Grey Grasshopper GRAS-03K2M-C CCD camera (Figure 4.3), together with a Mac mini, in order to set up a DIMM in addition to our self-built PSF seeing monitor.

Figure 4.3. The Point Grey Grasshopper GRAS-03K2M (for DIMM measurements) and GRAS-20S4M (for PSF seeing monitor measurements) CCD cameras.



Although the GRAS-03K2M, an interline-type CCD camera, has a very high frame rate of 200 frames per second (fps), it possesses a small number of pixels in its pixel array and would therefore not provide a sufficient FOV for the purposes of the PSF seeing monitor. In order to accommodate the IEEE1394 Firewire and Mac mini requirements of the DIMM setup, it was decided to compromise with respect to CCD type for the PSF seeing monitor and acquire an interline-type CCD camera, the Point Grey Grasshopper GRAS-20S4M (highlighted in green at the top of Table 4.2, also shown in Figure 4.3), which provides a larger number of pixels and a reasonably high frame rate of 30 fps.

A webcam, the Philips ToUcam Pro II PCVC840K (Figure 4.4), a colour camera with a high frame rate but a small number of pixels in its pixel array, was acquired previously to be used in an initial binary star observation test setup for the PSF seeing monitor (Figure 4.5). Webcams allow for very short exposure times. It would be possible to modify the ToUcam to become a monochrome camera by replacing its colour chip, the SONY ICX098BQ, with the black and white version thereof, the SONY ICX098BL. An Orion StarShoot USB Live View Value Kit (Figure 4.6) was acquired to assist in centering and focusing of the star image. It includes a flip mirror to visually find, center and focus the star image as well as a StarShoot USB eyepiece which transmits the image to the laptop.



Figure 4.4. The Philips ToUcam Pro II PCVC840K webcam with lens removed and replaced by MOGG adapter.



Figure 4.5. Test setup for double star observation – 10" Meade LX200 SCT, ToUcam webcam and laptop.



Figure 4.6. The Orion StarShoot USB Live View Value Kit with imaging flip mirror and StarShoot USB eyepiece.

### 4.3.3. Mount

The 14" Meade LX200 GPS SCT that was acquired comes with an alt-az fork-arm mount. Although fork-arm mounts are not ideal for imaging, the intention is to test the image quality delivered by this telescope with its heavy-duty alt-az fork-arm mount and field tripod before purchasing a high-quality GEM. As described previously, by fitting an equatorial wedge, the fork mount can be turned into a polar mount, eliminating field rotation. The short exposure images required by the PSF seeing monitor should eliminate telescope tracking errors and preclude the need for a field de-rotator, auto-guider or an equatorial mount. If the experience of the South African Astronomical Observatory (SAAO) South African Large Telescope (SALT) Site Monitoring Team with their MASS (Multi-Aperture Scintillation Sensor) - DIMM (Differential Image Motion Monitor) 10" Meade LX200 SCT on an alt-az fork-arm mount is anything to go by, however, an equatorial mount with guiding is more or less mandatory for DIMM imaging. At first, they used an equatorial wedge to turn their alt-az mount into a polar mount. During system automation, problems were encountered with computer controlled guiding and slewing using the Meade Autostar II control system. They replaced the mount with an A-P 900GTO mount, which provided much improved tracking in automated mode.

Even a mechanically, electrically and electronically sound mount will still suffer from wind buffeting (Starizona, 2000). A polar mount with guiding is therefore more or less mandatory for CCD imaging. High-quality telescope mounts such as those made by Astro-Physics and Software Bisque are known for rigidity, high pointing accuracy, smooth and accurate tracking as well as advanced GOTO capability and computer interfacing. A selection of commercially available GE mounts identified as being of sufficient quality for seeing monitor requirements is presented in Table 4.4.

The Astro-Physics (A-P) 900GTO and 1600GTO and Software Bisque (SB) Paramount MX are top quality mounts. The Losmandy HGM Titan mount is of slightly higher quality than the Celestron CGE Pro and Meade LX800 GE mounts, the latter being a recent addition of a GEM to the Meade brand of mostly fork-arm mounts. All the mounts come with mount calibration and modelling circuits or specialised software for Periodic Error Correction (PEC) to improve polar alignment and pointing precision etc. The Meade

LX800 GE additionally offers StarLock, which makes use of two auto-guiding cameras to refine the pointing and assist with alignment, target acquisition and guiding corrections.

Table 4.4. Comparison of telescope mounts.

| Mount                        | Astro-Physics |            | Software Bisque | Meade        | Losmandy   | Celestron    |
|------------------------------|---------------|------------|-----------------|--------------|------------|--------------|
| Model                        | 1600GTO       | 900GTO     | Paramount MX    | LX800 GEM    | HGM Titan  | CGE Pro      |
| <b>Instrument payload</b>    | 90 kg         | 31 kg      | 40 kg           | 40 kg        | 45 kg      | 40 kg        |
| <b>Counterweights incl.</b>  | No            | No         | 2x 9 kg         | 8 kg         | 2x 9.5 kg  | 10 kg        |
| <b>SCT apertures</b>         | > 18"         | > 12"      | > 14"           | > 14"        | >14"       | >14"         |
| <b>Price</b>                 | \$11700       | \$8750     | \$8995          | \$7299       | \$5995     | \$4999       |
| <b>Imaging past meridian</b> | Well past     | Well past  | 2 h             | 20 deg       | ?          | 20 deg       |
| <b>Latitude range</b>        | 0° - 78°      | 20° - 68°  | 10° - 65°       | ?            | 12° - 70°  | 10° - 65°    |
| <b>Pointing accuracy</b>     | < 1'          | < 1'       | 30"             | 1'           | 1'-2'      | 1'           |
| <b>Periodic Error (PE)</b>   | 5"            | 7"         | 7"              | ?            | 5"         | 3"           |
| <b>PE Correction (PEC)</b>   | PEMPro        | PEMPro     | 1", TPoint      | 1", StarLock | < 2"       | PPEC         |
| <b>Control software</b>      | PulseGuide    | PulseGuide | MKS5000         | AustoStar II | Gemini 2   | NexRemote    |
| <b>Power requirements</b>    | 12 V / 5 A    | 12 V / 5 A |                 | 12 V / 5 A   | 12 V / 3 A | 12 V / 3.5 A |
| <b>Servo drive system</b>    | DC            | DC         | DC              | DC           | DC         | DC           |
| <b>Mount weight</b>          | 52.5 kg       | 24.5 kg    | 23 kg           | 35 kg        | 34 kg      | 34 kg        |
| <b>Tripod incl.</b>          | No            | No         | No              | Yes          | No         | Yes          |

In choosing the most appropriate mount from the selection of GEMs, the mount's payload capacity should be matched to the weight of the instrument payload it would be expected to carry. The instrument payload currently anticipated is as follows:

- Meade LX200 14" GPS SCT of 27 kg;
- finder scope of < 1 kg;
- Point Grey GRAS-20S4M-C CCD camera of 104 g;
- Point Grey GRAS-03K2M-C CCD camera of 104 g;
- PhilipsToUcam PCVC840K webcam of 100 g;
- Orion StarShoot USB Live View Value Kit of < 1 kg;
- DIMM mask and prism of < 1 kg;
- instrument mounting interfaces and adapter plates of < 2 kg
- and instrument housing of < 1 kg,

therefore requiring a mount with a payload capacity of less than 35 kg.

However, the generally accepted view is that, for imaging purposes, a mount should carry far below its rated payload. The A-P 900GTO has a recommended SCT aperture diameter of 12" and a rated payload capacity of only 31 kg, which excludes it from further consideration. The SB Paramount MX, Celestron CGE Pro and Meade LX800 GEMs with payload capacities of 40 kg appear to be borderline cases, while the Losmandy HGM Titan with its payload capacity of 45 kg is able to handle only a few additional kilograms. Considering instrument capacity alone, the A-P 1600GTO is the only mount that meets the requirement of being able to carry well below its rated payload.

#### **4.4. Software and automation**

Once the final location of the seeing monitor has been decided, the system must be able to operate autonomously. A robotic system will be put in place with the master control system controlling the entire observatory – operation of the telescope, CCD camera, enclosure as well as the processing and communications computer. Observatory automation software allowing for automated control and remote monitoring of the observatory will have to be developed. The following tasks must be performed autonomously:

- the mount must be able to point the telescope with high accuracy towards the star and allow the telescope to accurately track;
- exact focus must be achieved;
- the CCD camera must be able to complete an entire acquisition session successfully;
- images must be processed and evaluated;
- seeing monitor measurements must be made available;
- the mount, CCD camera and computer must be turned on/off;
- the telescope must be parked;
- air conditioning units and ventilation fans must be controlled;
- the roof of the telescope enclosure needs to close automatically in the event of imminent bad weather;
- the status of weather and observatory conditions must be reported.

The master control system must control and integrate the functioning of all these subsystems and tasks without the necessity for human intervention and must therefore be flexible and robust.

#### **4.5. Logistical issues**

During the initial phase, a portable seeing monitor setup will be used to measure seeing conditions at various locations on-site. Once the location offering the best seeing conditions has been determined, a seeing monitor observatory will be established at this location, in close proximity to the LLR.

An access road, water, electricity and communications will be available at the location of the LLR but will be lacking for the various on-site locations during the initial monitoring of seeing conditions. Rough terrain will have to be traversed to reach these locations on ridges and koppies, requiring the use of an off-road vehicle and a very portable seeing monitor. The portable seeing monitor will not require access to water as there will be no cooling systems involved. A means of communication will also not be required for the relatively short seeing campaigns at the various on-site locations as all data will be stored to a laptop computer. Solar power will be required to provide electricity for the seeing monitor and a laptop computer.

Stable piers will have to be erected on which to mount the portable seeing monitor at the various on-site locations. The portable seeing monitor will be well-protected from wind by screens and from rain by a waterproof covering. The observatory seeing monitor will be housed in an enclosure built in close proximity to the LLR but as far as possible from local sources of bad seeing. This enclosure will consist of either a building with a roll-off roof or a motorised canvas clamshell dome (Figure 4.7). A stable platform isolated from vibrations will be erected so that the seeing monitor may operate from the same height above ground level as the LLR telescope (Figure 4.8).



Figure 4.7. The Cerro Tololo Inter-American Observatory (CTIO) Robo-DIMM in Chile with motorised canvas clamshell enclosure (source: CTIO).



Figure 4.8. The Isaac Newton Group of Telescopes (ING) – Instituto de Astrofísica de Canarias (IAC) RoboDIMM with Astro Haven fibreglass clamshell at the Observatorio del Roque de los Muchachos (ORM) La Palma, Canary Islands (source: Javier Méndez, ING).

#### 4.6. Target instrumentation

During a short intensive seeing campaign at the SAAO site in Sutherland in August 2011, the SALT combined MASS-DIMM instrument was calibrated against their Generalized Seeing Monitor (GSM) and Profileur de Bord Lunaire (PBL) by staff of the Laboratoire Hippolyte Fizeau of the Université de Nice Sophia-Antipolis. Three different optical remote sensing instruments were therefore employed simultaneously to measure optical parameters and turbulence profiles. This made it possible to cross-correlate SALT MASS-DIMM results with those from the GSM and PBL for verification, validation and calibration of the SALT MASS-DIMM. Combining the three different techniques provided for instruments complementing each other. The entire atmosphere could be sampled at a higher resolution and a number of seeing parameters could be measured. A possibility exists that the GSM and PBL as well as a spare DIMM from SAAO could be made available for a short intensive site testing campaign at Matjiesfontein. For continuous monitoring of local meteorological parameters to be used in support of seeing measurements and turbulence modelling, an Automatic Weather Station (AWS) needs to be installed on-site, in close proximity to the seeing monitor. Techniques and



instrumentation currently employed as part of site characterisation to determine seeing and boundary layer conditions are briefly described in Appendix A4. Instrumentation, such as the DIMM, MASS, MASS-DIMM, GSM and PBL, that could become available for use during short seeing campaigns, are described in detail in Appendix A4.